UNIVERSITY OF CALIFORNIA, SAN DIEGO

Quantitative Fluorescence Microscopy: Applications in Digital Pathology for Breast Conservation Surgery

A dissertation submitted in partial satisfaction of the requirements for the degree of Doctor of Philosophy

in

Electrical Engineering (Nanoscale Devices & Systems)

by

David Townsend Martin

Committee in charge:

Professor Sadik Esener, Chair
Professor Andrew Kummel, Co-Chair
Professor Michael Heller
Professor Yu-Hwa Lo
Professor Deli Wang

2011

The Dissertation of David Townsend Martin is approved, and is acceptable in quality and form for publication on microfilm and electronically:

Co-Chair

Chair

University of California, San Diego

2011

DEDICATION

I would like to dedicate this dissertation to my father, who fostered my love of science from an early age by writing “Science Letters for David” during the Gulf War and answering everyone question I ever thought of, to my mother for getting me started on the right foot in school and always being there to lend me help when I needed it, to my dear friend Trista Kang for keeping me in good spirits and putting a smile on my face through many long days of data analysis and long nights of cleanroom work, and to all my friends and family for your love and support over the years. Thank you all.

-David

TABLE OF CONTENTS

LIST OF FIGURES

LIST OF TABLES

ACKNOWLEDGEMENTS

I would like to acknowledge my thesis adviser, Professor Andrew Kummel for his support and guidance throughout my tenure in graduate school. His advice and professional demeanor were instrumental in keeping my research both progressing and interesting.

I would also like to acknowledge my colleagues in Kummel Lab, Messmer Lab, the Nano3 staff, and the other members of my PhD committee. Your support, through experimental help and discussion, contributed immensely to my success.

Chapter 1, in full, is a reprint of the material as it appears in Annals of Surgical Oncology, vol 16, 2009, Cortes-Mateos, Maria Jose; Martin, David; Sandoval, Sergio; Ruidiaz, Manuel E.; Messmer, Davorka; Wang-Rodriguez, Jessica; Trogler, William; Kummel, Andrew C.; Blair, Sarah L. The dissertation author was the principle graduate student researcher and author of this paper.

Chapter 2, in full, is a reprint of the material as it appears in Acta Cytologica, vol. 55, 2011, Martin, David T.; Sandoval, Sergio; Ta, Casey N.; Ruidiaz, Manuel E.; Cortes-Mateos, Maria Jose; Messmer, Davorka; Kummel, Andrew C.; Blair, Sarah L.; Wang-Rodriguez, Jessica. The dissertation author was the primary researcher and author and author of this paper.

Chapter 3, in full is currently being prepared for submission for publication of the material. Martin, David T.; Ta, Casey N.; Sandoval, Sergio; Ruidiaz, Manuel E.; Messmer, Davorka; Kummel, Andrew C.; Blair, Sarah L.; Wang-Rodriguez, Jessica. The dissertation author was the primary researcher and author of this material.

Chapter 4, in full, is a reprint of the material as it appears in Material Research Society Symposium Proceedings, vol. 1346, 2011, Martin, David T.; Sandoval, Sergio; Carter, Andy; Rodwell, Mark; Smith, Stefan G. Llewellyn; Kummel, Andrew C.; Messmer, Davorka. The dissertation author was the primary researcher and author of this material.

VITA

2003-2006	Computer Engineer, Scripps Institute of Oceanography
2006	Bachelor of Arts, Economics, University of California, San Diego
2006	Bachelor of Science, Computer Engineering, University of California, San Diego
2008	Masters of Science, Electrical Engineering (Nanoscale Devices & Systems), University of California, San Diego
2006-2011	Graduate Student Researcher, Nanomedicine Laboratory, University of California San Diego
2011	Doctor of Philosophy, Electrical Engineering (Nanoscale Devices & Systems), University of California, San Diego

PUBLICATIONS

M. J. Cortes-Mateos, D. T. Martin, S. Sandoval, M. E. Ruidiaz, D. Messmer, J. Wang-Rodriguez, W. Trogler, A. C. Kummel, S. L. Blair, "Automated Microscopy to Evaluate Surgical Specimens Via Touch Prep in Breast Cancer", Annals of Surgical Oncology, 2008

J. Yang, S. Sandoval, J. G. Alfaro, S. Aschemeyer, A. Liberman, D. T. Martin, M. Makale, A. C. Kummel, W. C. Trogler."Red-luminescent Europium (III) Doped Silica Nanoshells: Synthesis, Characterization and Their Interaction with HeLa Cells", Journal of Biomedical Optics, 2011

D. T. Martin, S. Sandoval, C. N. Ta, M. E. Ruidiaz, M. J. Cortes-Mateos, D. Messmer, A. C. Kummel, S. L. Blair, J. Wang-Rodriguez, "Quantitative Automated Image Analysis System with Automated Debris Filtering for the Detection of Breast Carcinoma Cells", Acta Cytologica, 2011

M. E. Ruidiaz, M. J. Cortes-Mateos, S. Sandoval, D. T. Martin, J. Wang-Rodriguez, F Hasteh, A. Wallace, J. G. Vose, A. C. Kummel, S. L. Blair, "Quantitative comparison of surgical margin histology following excision with traditional electrosurgery and a low-thermal-injury dissection device", Journal of Surgical Oncology, 2011

D. T. Martin, S. Sandoval, A. Carter, M. Rodwell, S. L Smith, A. C. Kummel, D. Davorka Messmer, "Fabrication of Silicon on Borosilicate Glass Microarrays for Quantitative Live Cell Imaging", Material Research Society Symposium Proceedings, Vol. 1346, 2011.

ABSTRACT OF THE DISSERTATION

Quantitative Fluorescence Microscopy: Applications in Digital Pathology for Breast Conservation Surgery

by

David Townsend Martin

Doctor of Philosophy in Electrical Engineering (Nanoscale Devices & Systems)

University of California, San Diego, 2011

Professor Sadik Esener, Chair

Professor Andrew Kummel, Co-Chair

Approximately a third of all breast conversation therapy patients require follow-up procedures due to positive margins in their final pathological diagnosis. While manual intraoperative evaluation of margin status can greatly reduce the need for secondary procedures, it requires detailed analysis by a highly skilled pathologist inside the operating room for accurate results. This dissertation documents the development of an automated approach to detect cancerous epithelial cells and evaluate fluorescently stained imprint cytology slides taken from excised breast tissue. By digitizing whole slide images and developing custom software algorithms to distinguish epithelial cells from debris and imaging artifacts, the presence of invasive

cancer was detected with 95% accuracy with no false positives when validated against the diagnosis of a highly experienced pathologist. While the difference between a cluster of cells and an air bubble or fiber is readily apparent to the human eye, a digitized microscopy system required training to recognize subjects of interest in slide images. Performing statistical measurements of the fluorescent properties of objects revealed intrinsic differences between cells and debris that could not be appreciated when focusing on intensity alone. Using these measurements to train an algorithm to correctly identify epithelial cells was crucial to the overall success of the technique. Accurately identifying fluorescently stained cells from a population of objects in a digitized image could be readily adapted to other clinical specimens beyond imprint cytology slides of breast tumor margins. This work demonstrates a proof of concept for developing a highly accurate and automated digital pathology system for intraoperatively evaluating margin status to guide surgical decisions, reduce pathologist workload, and lower positive margin rates. Lastly, an overview of a novel platform for analyzing single cell secretants through fluorescent imaging and development of a microfabrication process to produce it will be detailed.

INTRODUCTION

This dissertation represents the culmination of a multidisciplinary project between engineering students, cell biologists, practicing physicians, and biochemists to find a practical solution for evaluating margin status intraoperatively. We began with only a problem to solve: surgeons have only limited means to locate a tumor during excision, and principally rely on their gloved fingers to feel out an acceptable margin of healthy tissue to cut around the outside of a tumor. Since even a single cancer cell left behind can cause a recurrence of disease, removed tissue is sent off to a pathologist after surgery for microscopic analysis. Up to a third of the time, a pathologist will find cancer present in the margin area, which obviates the need for a secondary surgery for a wider clearance of tissue to be removed. To save both patients and surgeons from the hassle of multiple procedures, we began investigating automated methods to locate cancer cells present on the surface of excised tissue. After failing to find success in designing and fabricating complex microarrays to capture cells expressing various cancer markers, we shifted focus our focus to instead mimic what a pathologist does when diagnosing positive margins in breast conservation therapy: finding epithelial cells in places they do not belong. We began using adhesive slides to pull cells from tissue surfaces, and found that simply measuring epithelial cell density was a very strong indicator for the presence of cancer in breast tumor margins. Chapter 1 of this dissertation details the staining protocol that was used in all subsequent studies, and the development of a preliminary version of image processing software to automate cell counting in fluorescent microscope

images. The software results were compared against manual cell counting, as well as traditional permanent section analysis by a pathologist. The results of this initial study were highly encouraging. Chapter 2 details the further development of an automated image analysis program that could effectively screen out debris using predefined filters in images for more accurate cell counting. This debris filtering increased the overall accuracy to 94% when measured against diagnosis by a pathologist. Chapter 3 fully details the automation of debris filtering process using machine learning algorithms to increase the overall robustness of the technique, and enable its transferability to other automated systems and specimens. Chapter 4 diverges from the study of breast cancer surgery into building microenvironments for cell-cell communication. A fabrication process was developed to produce arrays of microwells with transparent bottoms to perform fluorescent imaging on cells over time. The automated image processing software and classification methods developed in Chapters 1-3 can now be adapted to perform automated measurements on live cells as they incubate inside these microwells in future work.

CHAPTER 1

Automated Microscopy to Evaluate Surgical Specimens Via Touch Prep in Breast Cancer

1.1 - ABSTRACT

Background: Breast conservation therapy is the standard treatment for breast cancer; however, 20–50% of operations have a positive margin leading to secondary procedures. The standard of care to evaluate surgical margins is based on permanent section. Imprint cytology (touch prep) has been used to evaluate surgical samples, but conventional techniques require an experienced cytopathologist for correct interpretation. An automated image screening process has been developed to discern cancer cells from normal epithelial cells. This technique is based on cellularity of the imprint specimen and does not require expertise in cytopathology.

Methods: A rapid immunofluorescent staining technique coupled with automated microscopy was used to classify specimens as cancer vs. non-cancer based on the density of epithelial cells captured on touch prep of tumor cross sections. The results of the automated analysis vs. a manual screen of ten 209 fields were compared to the pathology interpretation on permanent section.

Results: A total of 34 consecutive cases were analyzed: 10 normal cases, and 24 cancer cases. The cross section specimens for invasive cancer were correctly classified in at least 65% of the cases by using manual microscopy and at least 83% by using automated microscopy. The manual and automated microscopy correlated well for

measurements of epithelial cell density (R2 = 0.64); however, the automated microscopy was more accurate.

Conclusions: This preliminary study using an automated system for intraoperative interpretation does not require a cytopathologist and shows that rapid, low-resolution imaging can correctly identify cancer cells for invasive carcinoma in surgical specimens. Therefore, automated determination of cellularity in touch prep is a promising technique for future margin interpretation of breast conservation therapy.

1.2 - INTRODUCTION

Multiple, randomized, prospective trials with greater than a 10-year follow-up have proven that breast conservation therapy (BCT) has equal survival efficacy compared with mastectomy in treating early-stage breast cancer; therefore, BCT has become the standard of care to treat this malignancy [1-4]. Another important aspect of BCT is improved cosmetic outcome, because the best results are obtained at the time of the initial operation with a single excision and better aesthetic outcomes correlate with improved quality of life [5]. However, obtaining a negative margin in localized excision with primary BCT is still a challenge. Many studies show that local recurrence is significantly higher in patients with a positive margin vs. a negative margin excision [3, 6, 7]. Despite improved preoperative imaging techniques, such as breast MRI and ultrasound, many studies report positive margin rates of 20–50% for partial mastectomy, even for patients with early stage breast cancer. Therefore, achieving negative surgical margins is an essential goal in breast cancer treatment,

because the consequences of a failed margin are significant for patients, surgeons, and the healthcare system [8].

The ‘‘gold standard’’ for achieving negative margins for most tumors is performing multiple intraoperative frozen sections on the margins of the excised tumor. However, this technique has many limitations. Freezing the adipose tissue of the breast and preparing adequate and representative sections is a technically complex process [9]. Frozen-section evaluations on multiple samples from a three-dimensional cavity, while the patient and the surgeon are waiting for the results in the operating room, are extremely labor intensive and time consuming. In addition, there is concern that in small tumors the frozen sections may utilize the majority of the available tumor tissue and there will be insufficient specimens available for adequate histological evaluation and associated studies on permanent sections. The technique of using touch preps to detect tumor cells at breast cancer surgical margins has been studied during the last 20 years [10-12]. The largest study by Klimberg et al. [11] examined 428 patients with breast lesions and had a sensitivity of 96% and specificity of 100%. This group performed scrape and touch preps of a cross-section of the tumor as well as the marginal tissue around the tumor. The slides were fixed, stained with hematoxylin and eosin, and examined by an experienced cytopathologist. However, other institutions have not embraced this technique because artifacts associated with air drying and surface cautery can affect touch prep interpretation and the availability of an experienced cytopathologist limits its widespread use [9]. The objective of this project is to develop an automated real-time intraoperative technique to detect cancer cells present at surgical margins to prevent positive margins and the need for a second

operation to clear the microscopic margins. The long-term goal is to reduce the necessity of multiple operations to surgically treat breast cancer.

1.3 - METHODS

1.3.1 - Surgical Samples

Institutional Review Board approval from the University of California, San Diego, was obtained to study breast cancer and non-cancer tissue from patients. All patients underwent their planned procedure for breast surgical treatment, and the specimens were removed and sent to the pathology laboratory for analysis. Thirty-four consecutive cases, both cancerous (n = 24) and normal tissue (n = 10), were studied. The normal tissue was obtained from patients who underwent breast reduction or prophylactic mastectomy. All surgeries were performed at the University of California, San Diego. Standard techniques for resection of breast tissue were used, including electric cautery (Valley Labs, Boulder, CO). Fresh specimens were gently imprinted onto poly-L-lysine (PLL) coated glass slides (Newcomer Supply, Middleton, WI).

1.3.2 - Cross-Sections

To study the efficacy of the proposed technique in correctly identifying cancer cells in fresh surgical specimens by immunofluorescence (IF), the excised tissue was cut through the center to reveal the tumor (designated as ‘‘cross-section’’), and a touch prep of the cross-section was performed. The surgical specimens were grossed in by a surgical pathologist to locate the area with the highest probability of identifying tumor

cells. These cross-sectional cuts do not have a cauterized surface making them ideal specimen to establish the reliability and accuracy of the automated analysis technique on the most consistent available samples. The tissue was bisected and immediately imprinted/touched onto PLL slides to minimize air drying artifacts. For invasive carcinomas, the location of the tumor in the tissue was usually located by palpation; therefore, the cross-section nearly always bisected the tumor. For smaller tumors, such as ductal carcinoma in situ (DCIS), the location of the tumor was approximated by mammographic needle localization. However, many of the small tumors had been subjected to a previous core biopsy, which may have removed most of the cancer cells. The mammographers at University of California, San Diego, routinely use 9 to 11 gauge vacuum-assisted cores to establish a diagnosis.

1.3.3 - Immunofluorescence Staining

Two quantifiers were used to identify the cancer cells: (1) cytokeratin was used as a specific marker for epithelial cells to distinguish them from other cells that can be found attached to the PLL-slide after performing touch prep (leukocytes, adipocytes, fibroblasts, etc.); (2) cell density was quantified by using Hoechst 33342 (Invitrogen, Carlsbad, CA) as a nuclear dye. The Hoechst staining served several purposes: it enabled the exclusion of non-nucleated cells (e.g., erythrocytes), and facilitated counting the cells within clusters (**Figure 1.1**). Mouse IgG isotype control (Southern Biotechnology, Birmingham, AL) and anti-cytokeratin antibody (DakoCytomation, Carpinteria, CA) were labeled using the Alexa Fluor 488 Zenon Mouse IgG Labeling Kit (Invitrogen) following the manufacturer's instruction and kept in the dark at 4°C.

The slides were fixed with 4% paraformaldehyde (PFA) in phosphate-buffered saline (PBS) for 10 min at room temperature and rinsed by immersion in PBS. To reduce background from nonspecific binding of the antibodies to the cell Fc receptors, the samples were incubated at room temperature for 5 min with human IgG (10 µg/ml; Invitrogen) in PBS followed by washing by immersion in PBS. After blocking, the samples were permeabilized and stained in one step using the Inside Stain Kit (Miltenyi Biotec, Aubum, CA). AlexaFluor 488 labeled antibodies (mouse IgG isotype control and anti-cytokeratin) were diluted with Inside Perm reagent at 6 µg/ml and Hoechst at 10 µg/ml. The samples were incubated in the permeabilization-staining solution for 15 min at room temperature in the dark. Afterwards, the samples were washed by immersion in PBS. Finally, the slides were mounted with ProLong Gold (Invitrogen), a microscope cover glass was placed on the slide, and the slide was analyzed by microscopy. The complete staining protocol, including fixing, permeabilization, and blocking took only 20–25 min.

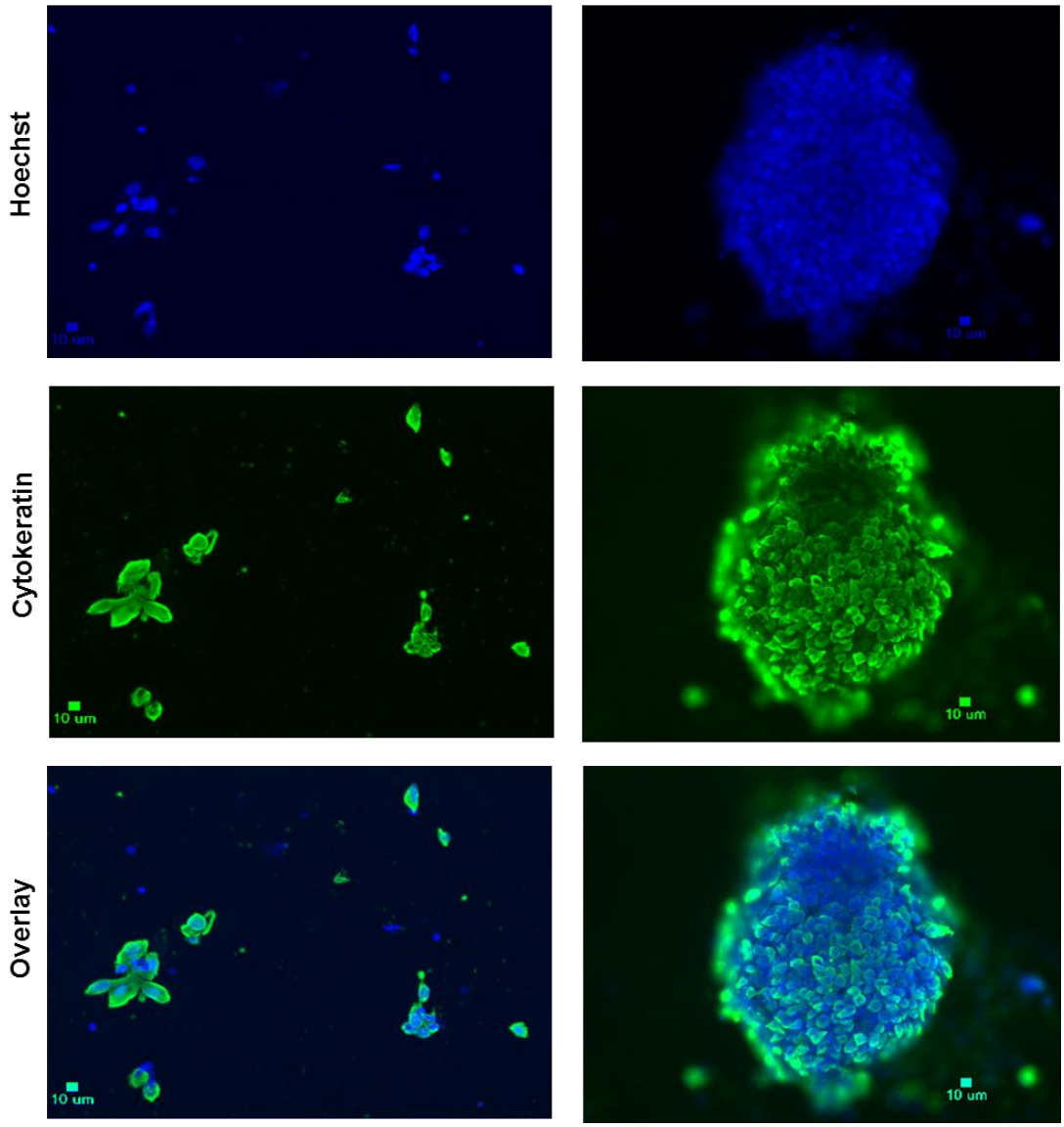

Figure 1.1: Immunofluorescence staining of touch-prep slides. Individual cells, small cell clusters and big cell clusters can be observed on the slide. Based on the number of epithelial cells and /or clusters, the slides are classified as positive or negative.

1.3.4 - Manual Analysis of the Slides

After staining, the slides were analyzed manually using a fluorescent microscope (Nikon Eclipse E600, Nikon Instruments Inc., Melville, NY) with a triple

bandpass filter (DAPI/FITC/Texas Red w/Single-Band Exciters, Chroma Technology Corp, Rockingham, VT). Ten fields close to the centerline of the slide were chosen and analyzed using a 209 objective. The total number of cells was obtained by counting all nuclei (Hoechst positive), and the number of epithelial cells was obtained by counting cytokeratin positive cells. Large three-dimensional clusters of epithelial cells were considered cancerous. The cell count for each large cluster was estimated by counting the number of nuclei in a fraction of each cluster and then correcting for the total area of the cluster. From the ten fields of view at 209 along the centerline of the long axis of the slide, both the number of epithelial cells/mm^2 (epithelial cell density) and the percentage of epithelial cells were calculated. It is noted that in this manual microscopy method, the choice of image fields was focused on the area of highest concentration of epithelial cells. The microscopist examined a progression of ten locations along the centerline. At each location, the field of view was adjusted in the local region (±300 lm) to image as many cells as possible. Therefore, it is expected that the manual microscopy method will measure a higher average epithelial cell density than the automated microscopy method, but there should be a strong correlation between the two measurements.

1.3.5 - Automated Microscopy and Analysis of the Slides

An automated scanning stage microscope was used for the data acquisition (AxioImager Z1, Carl Zeiss Inc., Thornwood, NY). In the automated microscopy analysis, the entire surface of each touch prep slide was imaged at a magnification of 5x with a 1.4 megapixel camera (Cool-SNAP HQ2, Photometrics, Pleasanton, CA);

the absolute resolution was 1.267 μm/pixel. A series of focus points for the slide was first determined manually along with appropriate exposure times for each fluorescent channel to maximize sensitivity to staining intensity. Afterwards, the automated microscope divided the slide into a series of tiles and recorded two fluorescent images (one for Hoechst fluorescence and one for cytokeratin fluorescence) at each of these tiles. Finally, the tiled images were loaded into a custom fluorescent image analysis program to specifically recognize both isolated cells and cells within tightly packed clusters. The cellular recognition software used an image tile of Hoechst fluorescence and an image tile of cytokeratin fluorescence at each location on the slide.

Each Hoechst image was used to determine how many non-epithelial cells were present in a given location and to filter out cytokeratin-positive artifacts. First, an estimation of background Hoechst fluorescence was determined for the image tile by sampling intensity values across 10% of the image tile. The mean and standard deviation of fluorescence intensity were calculated from this sampling set, and the intensity value one standard deviation below the mean was used as an estimate of background fluorescence for the image tile, and subtracted from all other pixels in that tile. Due to inherent variations of fluorescent staining across a slide, determining a distinct background value for each image tile was crucial. After background subtraction, median filtering was applied to the image tile to reduce grain noise while preserving edges. Next, contrast enhancement was performed to maximize the intensity difference between background staining and any positively stained cell nuclei in the image. Finally Otsu thresholding, a technique that enhances object outlines by separating foreground areas of an image from background areas, was performed on the

image tile to obtain binary outlines for any nuclei present [13]. After all image processing steps are complete, valid outlines of nuclei must be filtered out from any erroneous outlines of image artifacts. A Hoechst outline is determined to be a valid outline of a nucleus if its average Hoechst fluorescence is twice the background, the nuclear diameter is > 4.5 μm, and the circularity of the outline is > 0.6 for which 1 represents a perfect circle.

Automated interpretation of cytokeratin fluorescence was more complicated. Epithelial cells tended to be captured by touch prep in large clusters of cells, which were poorly penetrated by the anti-cytokeratin antibody. Poor antibody penetration and cell layering effects in clusters made it difficult to develop a universal algorithm using standard methods that could identify both single epithelial cells and each individual epithelial cell located inside of a cell cluster. Instead an algorithm was developed that finds a single outline for each cluster of epithelial cells as well an outline for each isolated epithelial cell. (**a**) Background subtraction on a tile by tile basis, as described in the Hoechst image procedure, was performed on each cytokeratin tile image to normalize intensity values to any background staining and a median filter was applied to reduce grain noise. (**b**) A hole-filling algorithm was used to fill in any weakly stained areas between cells located in a cluster that would otherwise cause fragmented outlines. The hole-filling algorithm has no effect on single cells because it only smooths fluorescent intensity across a cell's cytoplasm. (**c**) A Sobel edge enhancement (a technique that enhances edges in an image by differentiating the intensity gradient in a radius around each pixel) was performed to convert the image into a binary representation of the edges of all cells and clusters

present [14]. (**d**) The edge representation was slightly dilated to compensate for any information loss in the previous steps. (e) A hole-filling was performed once more before Otsu thresholding to determine final single epithelial cell and epithelial cell cluster outlines for an image. (f) The area occupied by each epithelial cell cluster was calculated. By dividing each cluster area by the average size of an epithelial cell (200 lm2), an approximation for the total number of epithelial cells in each cluster was obtained (**Figure 1.2**). Note that this method assumes all clusters occupy a two-dimensional plane, thereby undercounting the number of epithelial cells in multilayer clusters. Epithelial cell outlines were checked for validity before being used in the statistical analysis. Raw cytokeratin outlines obtained from the image processing steps are filtered to have a nuclear area of at least 15 μm^2, an average cytokeratin fluorescence twice that of the background cytokeratin fluorescence of the image tile, and an average Hoechst fluorescence intensity greater than the background Hoechst intensity of the image tile to ensure accepted cytokeratin outlines contain cell nuclei and thus represent epithelial cells. The automated microscopy currently requires 45 min to scan an entire slide with a 5x objective and a 1.4 megapixel camera; with a 14 megapixel camera, this will be reduced to less than 5 min. The current microscope requires 15 min of setup time, because it does not have a practical auto-focusing system. By using a larger camera, a lower magnification objective can be used to maintain a fixed imaging resolution, which will reduce the time required for auto focusing to less than 1 min with efficient software.

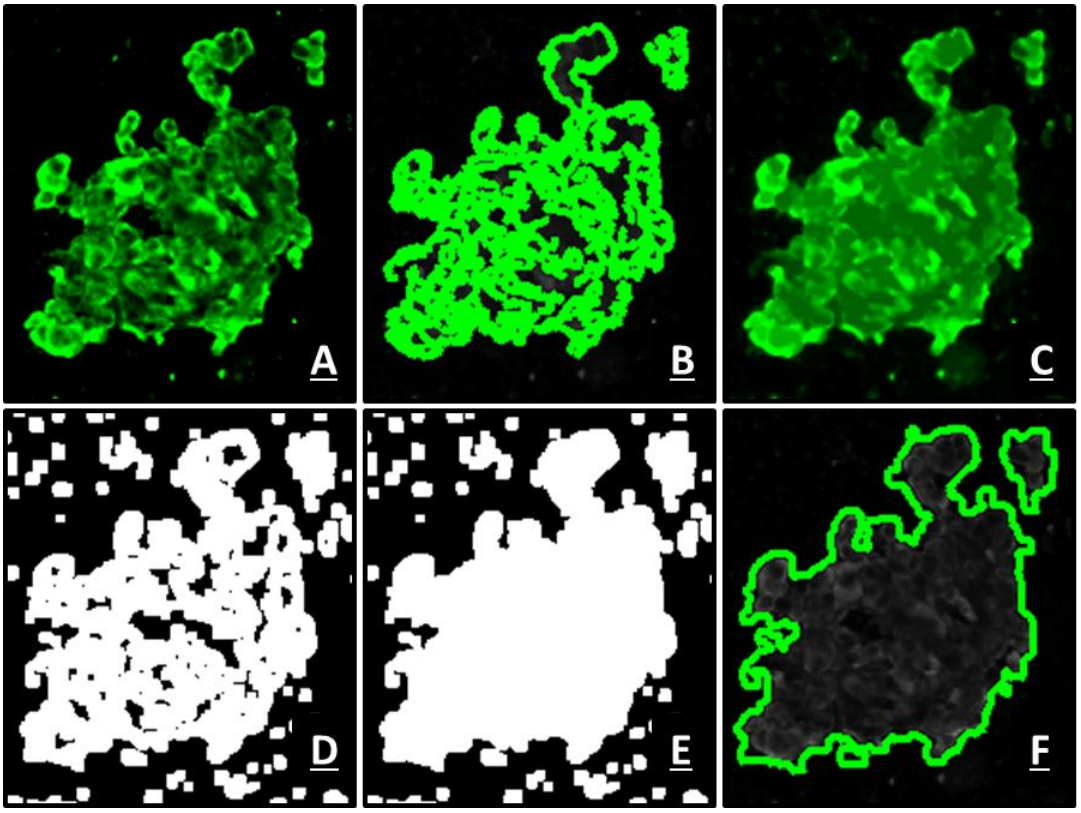

Figure 1.2: Automatic microscopy algorithm. **A)** Background subtracted Cytokeratin Fluorescence image tile. **B)** Fragmented outlines resulting from standard outlining techniques **C)** Median Filtering and Hole Filling **D)** Sobel Edge enhancement and dilation **E)** Hole Filling **F)** Final epithelial outlines overlain on original image tile.

1.3.6 - Statistics

Automated and manual microscopy were correlated with Pearson's correlation. Cutoff values between benign and malignant cells were calculated based on Fisher linear discriminant analysis [15].

1.4 - RESULTS

Patient Profiles Thirty-four consecutive surgical samples were analyzed (from August 2007 to April 2008). Ten of these samples were noncancerous tissues (6 from breast reduction and 4 from prophylactic mastectomies), and 24 samples were breast cancer with differing diagnostic classifications (6 DCIS; 14 invasive ductal carcinoma (IDC); 1 lobular carcinoma in situ (LCIS), and 3 invasive lobular carcinoma (ILC)). The 14 cases of IDC were subclassified as follows: 7 (50%) were only IDC, 4 (29%) were IDC/DCIS, 2 (14%) were IDC with lobular features, and 1 (7%) was IDC/LCIS. Thirteen patients underwent mastectomies and 11 underwent lumpectomy or BCT (**Table 1.1**). One to five serial touch prep slides of cross-sections were analyzed for each sample. The touch prep results were compared to final evaluation of the entire specimen by the pathologists at the University of California, San Diego.

Table 1.1: Patients demographic information, including the age, diagnosis and pathological data obtained from Pathology Laboratory (L=Lumpectomy; M=Mastectomy; BR=Breast Reduction; PM=Prophylactic Mastectomy; DCIS= Ductal Carcinoma in situ; IDC= Invasive Ductal Carcinoma; LCIS=Lobular Carcinoma in situ; ILC=Invasive Lobular Carcinoma; N=Normal)

SAMPLE	AGE	SURGERY	DIAGNOSIS	GRADE	STAGE
C1	46	L	DCIS	2	0
C2	58	L	DCIS	2	0
C3	56	M	DCIS	3	0
C4	57	M	DCIS	2	0
C5	64	M	DCIS	3	0
C6	59	L	DCIS/LCIS	3	0
C7	49	L	IDC	2	I
C8	49	L	IDC	3	III
C9	52	L	IDC	3	I
C10	70	L	IDC	3	I
C11	42	M	IDC	2	I
C12	49	M	IDC	3	III
C13	86	M	IDC	2	II
C14	58	L	IDC/DCIS	2	II
C15	59	L	IDC/DCIS	2	I
C16	41	M	IDC/DCIS	3	I
C17	58	M	IDC/DCIS	2	I
C18	48	L	IDC/ILC	2	III
C19	68	L	IDC/ILC	1	II
C20	40	M	IDC/LCIS	1	I
C21	49	M	LCIS	2	0
C22	40	M	ILC	2	II
C23	56	M	ILC	2	III
C24	49	M	ILC	2	I
N1	18	BR	N		
N2	23	BR	N		
N3	26	BR	N		
N4	30	BR	N		
N5	47	BR	N		
N6	71	BR	N		
N7	56	PM	N		
N8	41	PM	N		
N9	42	PM	N		
N10	43	PM	N		

1.4.1 - Analysis of Multiple Cross-Sectional Cuts

The density of epithelial cells in the cross-section slides of normal and cancer samples were compared by using the manual counting method vs. automated microscopy. An example of this technique is shown in **Figure 1.3a**; manual microscopy for case C14 contained a 5x2 cm tumor in a 8x6x5 cm tissue sample. Slices 1, 2, and 3 had an epithelial cells density more than tenfold greater than slices 4 and 5, consistent with the touch prep method accurately locating the tumor. The edges of the tumor had fewer cells captured than the center of the tumor. To determine the probability of sampling the tumor and the expected variation of epithelial cell density along the total tissue sample, serial cross-section sampling (with 2 to 5 serial cuts) was performed in 20 samples (13 cancer and 7 normal samples). To estimate the variation of epithelial cell density between all cuts for a given tissue sample, the minimum number of cells per mm^2 on a single cut was divided by maximum number of cells per mm2 on a single cut. As shown in **Figure 1.3b**, most normal cases have a ratio close to 1.

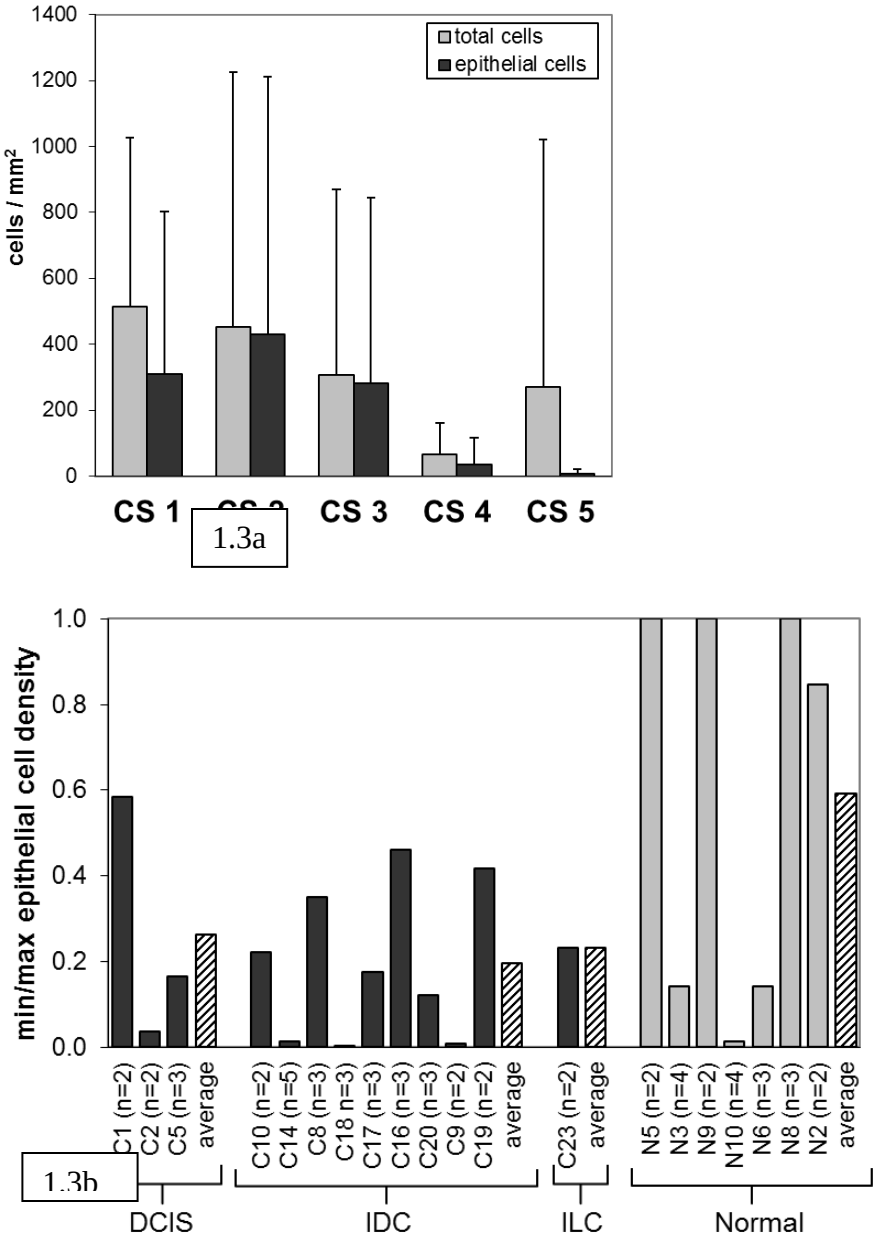

Figure 1.3: Serial sections of cross section of tumor. **A.** Five serial cross-section slides of a surgical sample were done. We found that the highest density of cells attached to slides 1, 2 and 3,the center of the palpable tumor. **B.** Ratio of epithelial cells (minimum divided by maximum number of epithelial cells on the serial cross-section slides) per sample. Cross-sectional slides were done in cancer and normal samples; the number of cross-sectional slides (n) varies from 2 to 5 showing a large variation in cell density depending in which area of the tumor was touched onto PLP coated slides

In three normal cases, the ratio was lower, which was attributed to high adipose breast tissue in patients who underwent breast reduction operations. For IDC and DCIS, the ratio of maximum to minimum epithelial cells can be very low, consistent with a high probability of missing the tumor in a single random cut. For invasive tumors, the probability of bisecting the tumor in a cross-section tissue cut was high, because the tumors studied were usually palpable and large (average tumor size in cm: IDC = 2 ± 1.3; ILC = 3.1 ± 2.7). Conversely, noninvasive carcinomas are more difficult to sample in cross-sectional tissue cuts because these tumors are smaller (DCIS = 1.1 ± 0.7 cm) and rarely palpable. To determine the accuracy of the tumor detection technique, the probability of missing the tumor in a cross-sectional cut in the absence of palpation was estimated from the ratio of Feret's diameters of the tumors and tissue. Feret's diameter is the longest distance between any two points of an outline. For a single slice, the probability of missing the tumor (p) is a linear function of the relative diameters of the tissue (d_{tissue}) and the tumor (d_{tumor}): $p = 1 - d_{tumor}/d_{tissue}$. When multiple slices are taken, the probability of missing the tumor is lowered as a power function of the number of slices (n). Probability of missing the tumor for n slices = $p^n = (1 - d_{tumor}/d_{tissue})^n$. The probability of missing a tumor inside a surgical sample when ''n'' cuts were performed (p^n) was calculated for all samples (**Table 1.2**). For DCIS, the average probability of missing the tumor is 87.5%; therefore, DCIS should only be observed by the cancer detection techniques for 12.5% of the cases if the cross-section cuts are completely random. For invasive cancers (IDC + ILC), the average probability of missing the tumor is only 65% because the tumor

sizes are larger than for DCIS; invasive cancer should only be observed by the cancer detection techniques for 35% of the cases if the cross-section cuts are completely random. Therefore, in the reported numbers for sensitivity of the manual and automated cellularity touch prep technique are always reported as minimum sensitivity, because it is hypothesized that some of the negative scores are solely due to the tumor not being sampled.

Table 1.2: Data of tumor and sample size, ratio between them and probability of missing the tumor when serial cross-section slides where done (CS=cross-section; ($p^n = (1 - [d_{tumor} / d_{sample}])^n$; *n = number of CS slides*).

SAMPLE	SURGERY	DIAGNOSIS	C-S Slides	SAMPLE SIZE (cm)	TUMOR SIZE (cm)	d_{Tumor} / d_{Sample}	p^n
C2	L	DCIS	2	6 x 4.5 x 1.5	0.6	0.10	0.81
C5	M	DCIS	3	27 x 19.5 x 4	1.5	0.06	0.84
C6	L	DCIS/LCIS	1	6.4 x 4.2 x 1.3	1	0.16	0.84
C1	L	DCIS	2	5.4 x 4.6 x 1.6	0.3	0.06	0.89
C4	M	DCIS	1	23 x 19.5 x 9	2.3	0.10	0.90
C3	M	DCIS	1	23 x 20 x 6	0.8	0.03	0.97
C18	L	IDC/ILC	3	5.5 x 4.5 x 1.9	5.5	1.00	0.00
C14	L	IDC/DCIS	5	8 x 6 x 5	2.5	0.31	0.15
C8	L	IDC	3	5.3 x 5 x 2.5	2.1	0.40	0.22
C17	M	IDC/DCIS	4	17 x 11 x 3.2	2.8	0.16	0.49
C10	L	IDC	2	5 x 7 x 2.5	2	0.29	0.51
C15	L	IDC/DCIS	1	4.5 x 3 x 1.5	2	0.44	0.56
C19	L	IDC/ILC	2	7.5 x 4.6 x 2.5	1.5	0.20	0.64
C7	L	IDC	1	6.1 x 4 x 1.5	1.2	0.20	0.80
C9	L	IDC	2	11 x 8 x 3	1	0.09	0.83
C12	M	IDC	1	17.5 x 17 x 5	3	0.17	0.83
C16	M	IDC/DCIS	3	13.5 x 13 x 3	0.8	0.06	0.83
C13	M	IDC	1	19.5 x 19 x 5.5	3	0.15	0.85
C20	M	IDC/LCIS	3	17.5 x 12 x 3	0.2	0.01	0.97
C11	M	IDC	1	23 x 17 x 3	0.7	0.03	0.97
C21	M	LCIS	1	14.5 x 14 x 5.3	----	0.00	1.00
C23	M	ILC	2	25 x 16 x 35	6	0.24	0.58
C22	M	ILC	1	16.5 x 13.5 x 7	2.6	0.16	0.84
C24	M	ILC	1	15.5 x 13 x 6	0.7	0.05	0.95

1.4.2 - Manual Analysis of Cross-Sectional Cuts

For manual microscopy, we utilized the highest density of epithelial cells (**Figure 1.4a**) as well as the fraction of epithelial cells as a marker of cancer. Both parameters were used to separate cancer vs. non-cancer because the manual microscopy only samples less than 5% of the surface of the slide. For cases in which there are multiple cross-sectional cuts, the data from the slide with the highest cell density as determined by manual microscopy is reported. In touch prep, the tumor was pressed on the slide with minimal smearing; therefore, cells were localized in specific regions on the slide occasionally causing a manual microscopy sampling error, but this potential error is minimized by using the slide with the highest cell density. From the data in **Figure 1.4a**, a decision boundary was drawn between cancer and non-cancer samples based on Fisher linear discriminant analysis. The outlier with more than 1,000 epithelial cells / mm^2 was excluded. The Fisher analysis cutoff line is diagonal consistent with both epithelial cells density and percent epithelial cells being useful quantifiers for identifying cancer cells in manual microscopy. Samples with more than 482 epithelial cells / mm^2 or more than 80% epithelial cells were considered tumor. Based on these criteria, 64.7% (11 cases) of the invasive cases (IDC + ILC) were correctly identified as containing cancer cells, and 35.3% (6 cases) were misclassified. The four cases of IDC incorrectly classified had very high probabilities of missing the tumor because they were small tumors with few cross-sectional cuts. The calculated probabilities for the different cases were: C11 $p^n = 0.97$, C12 $p^n = 0.83$, C15 $p^n = 0.56$, and C19 $p^n = 0.64$. In one of these cases, no cells were found on the slide after manual inspection, indicating that this specimen was most likely misprocessed. This

observation was confirmed by automatic analysis. For the three cases of ILC included in the study, only one was identified as cancer and two (C22 $p^n = 0.84$, and C23 $p^n = 0.58$) as normal. If all the invasive cases are combined, even in manual microscopy, which only samples 5% of the slide, at least 65% of the cases were correctly classified, which is double the 35% expected rate based on random cross-sectional cuts. For the six DCIS cases, 33.3% (2 cases) were correctly classified as cancer (C1 and C6), whereas four were missed (C2–C5).

1.4.3 - Automated Microscopy of Cross-Sectional Cuts

The entire touch prep glass slide was imaged at 5x with an automated microscope, and the number of epithelial cells/mm^2 as well as the percent epithelial cells present on the entire slide were calculated (**Figure 1.4b**). For cases in which there are multiple cross-sectional cuts, the data from the slide with the highest epithelial cell density as determined by automated microscopy is reported; note this can be different than the slide with the greatest epithelial cell density as determined by manual microscopy.

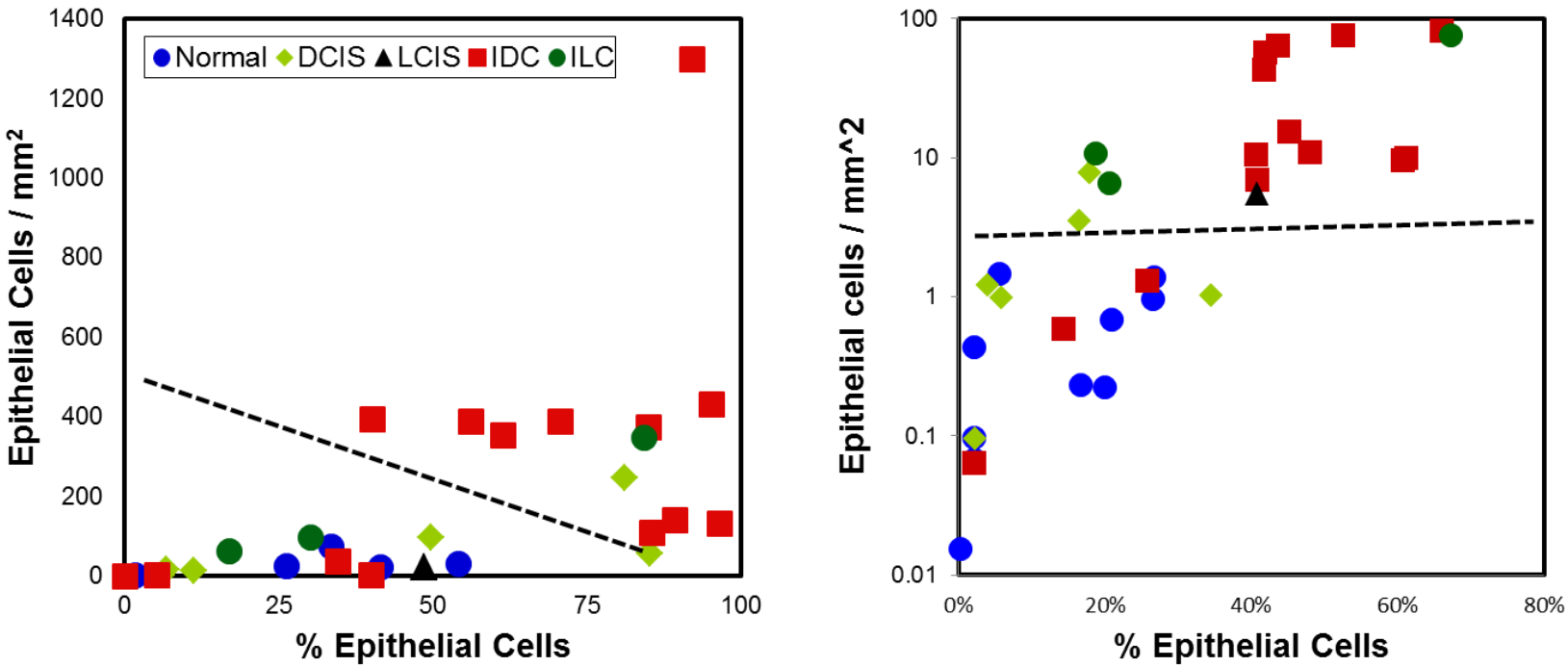

Figure 1.4: Manuel and Automated Analysis of cross sectional cuts. A. This graph shows the manual microscopy of 10 fields of view across the center line. For multiple cross sectional cuts, data from the slide with the highest epithelial cell density are displayed. High epithelial cell density or high percentage epithelial cells are consistent with cancer. **B.** This graph demonstrates the automated analysis. Our computer program counted the total epithelial within the entire slide. We had 80% accuracy in identifying invasive cancer.

Furthermore, it was observed that the density of epithelial cells is much lower in automated microscopy compared with manual microscopy because the latter only looks a 5% of the total slide, whereas automated analysis examines the entire slide surface and therefore includes many empty areas. The density of epithelial cells is plotted on a log-scale for the automated microscopy because the dynamics range is approximately two orders of magnitude greater than for manual microscopy. From the automated microscopy data in **Figure 1.4b**, a decision boundary was drawn between cancer and non-cancer samples based on Fisher's linear discriminant analysis, which included the data points closest to the cutoff line (cancer: epithelial cells/mm^2 between 3 and 20 and non-cancer: epithelial cells/mm^2 between 0.4 and 3). The Fisher analysis cutoff line (2.5 epithelial cells/mm^2) is consistent with only the epithelial cells density being required to differentiate cancer cells from non-cancer cells in automated microscopy. Based on this criterion, cancer was correctly classified in at least 17 (71%) cases overall: invasive plus pre-invasive. For invasive cancer cancers (IDC + ILC), three cases were misclassified giving an accuracy rate of 83%, which is 2.59x greater than the 35% expected rate based on random cross-sectional cuts. The automated microscopy was able to successfully detect all three ILC cases, which is important for surgeons because it is a challenge to obtain negative margins for ILC secondary to its diffuse spread throughout surrounding breast tissue [16]. The three cases of IDC incorrectly classified had high probabilities of missing the tumor, because they were small tumors with few cross-sectional cuts. The calculated probabilities of missing the tumor for the different cases were: C11 $p^n = 0.97$, C15 $p^n = 0.56$, and C19 $p^n = 0.64$. Note that these three IDC cases incorrectly classified by

automated microscopy are a subset of the four IDC cases missed in manual microscopy, consistent with manual sampling missing the tumor. For pre-invasive cancers (DCIS + LCIS), four DCIS cases were missed (C2, C3, C4, and C6). Two DCIS cases (C1 and C5) and one lobular carcinoma in situ (LCIS) were correctly classified, for an accuracy rate of 42.8% for in situ cancers, which is more than 39 the expected detection rate (12.5%) based on random cross-sectional cuts. Examining the total number of cells counted by automated microscopy (Table 3), it is noted that epithelial cell density is the most important factor to separate cancer vs. non-cancer. These results show that a nuclear stain alone cannot be used to successfully differentiate between prophylactic mastectomy tissue and cancerous tissue. The addition of an epithelial cell marker greatly enhances the ability to differentiate invasive carcinomas and lobular cancers from normal and prophylactic mastectomy tissue. Although the mean density of epithelial cells is 49 greater in DCIS than in normal samples, the standard deviation of the DCIS mean epithelial cells density (117%) is sufficiently large that even this 49 difference is not high enough to allow epithelial cells density alone to distinguish DCIS from normal in touch prep. Additional characteristics will need to be examined to increase the recognition of DCIS [17].

1.4.4 - Correlation of Automated and Manual Microscopy

To compare the manual and automated microscopy, the epithelial cell density and the fraction of epithelial cells were compared using the slide from the cross-sectional cuts with the highest epithelial cell density as reported by automated

microscopy. As shown in **Figure 1.5**, the automated microscopy of the entire slide correlated well with manual microscopic analysis of the ten centerline fields. For epithelial cell density and percentage of epithelial cells, R^2 values of 0.64 and 0.59 were observed respectively for correlation fits between automated and manual microscopy results. When few cells were present on a given slide, a poor agreement between manual counting of 5% of the slide and automated counting of the entire slide resulted in a large deviation from the trend line. In addition, even for IDC, there were occasionally cases in which a large deviation between manual and automated microscopy was observed, because manual microscopy only sampled a small fraction of the surface, which contained large cluster of cells.

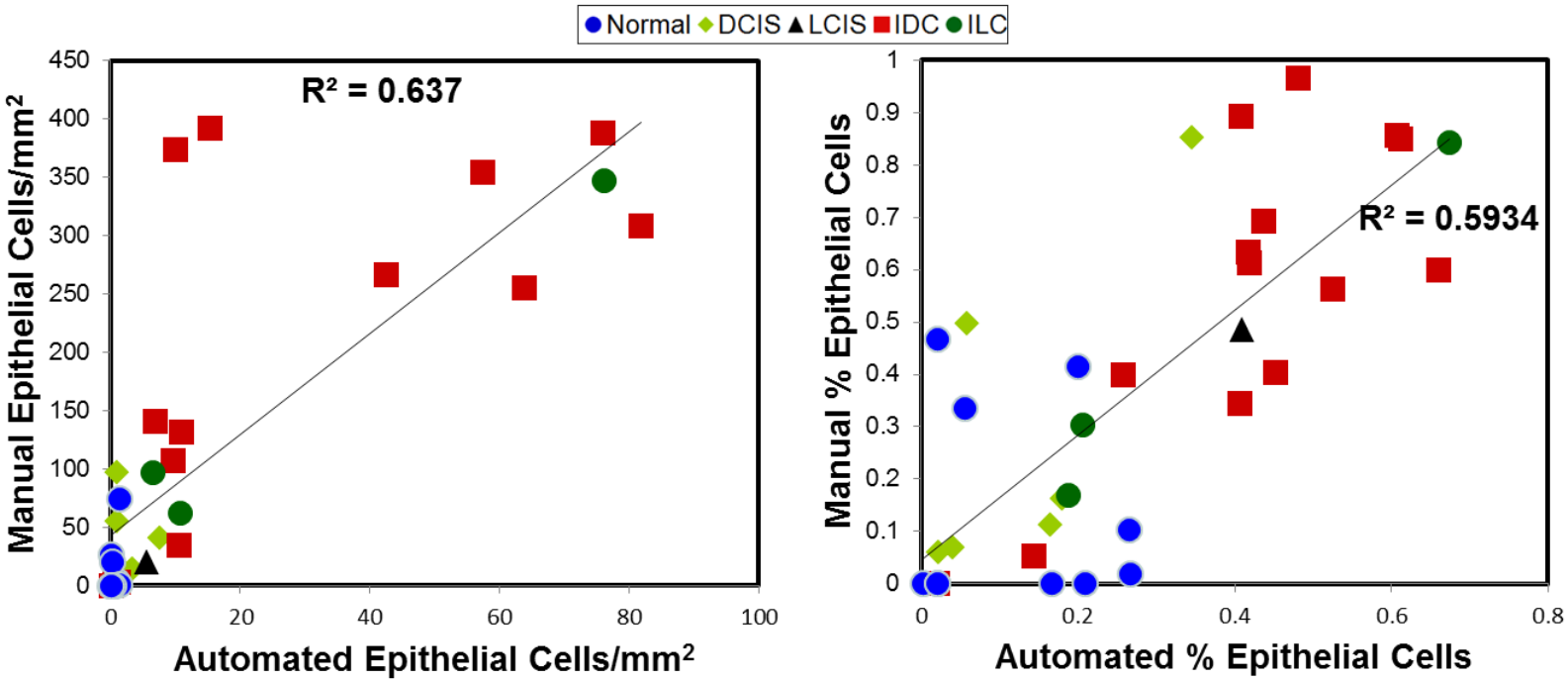

Figure 1.5: Correlation of manual vs. automated analysis of the cross sections of tumor. **A.** This graph shows a strong correlation between the manual and automated analysis based on cell density. For the manual analysis where only a fraction of the slide is analyzed there can be large variation when few cells are present on a slide. **B.** This graph shows the correlation between manual and automated analysis based on epithelial cell density

The sampling variation in manual microscopy is illustrated in **Figure 1.6**. Image tiles captured by the automated microscope were reanalyzed to mimic the manual microscopy method of examining only the centerline of a slide. All the cells were counted in each image tile and epithelial cell counts along horizontal image tile rows were summed. In slides of invasive cancers that contained large numbers of cells present in all parts of the slide, the manual and computer microscopy were equivalent. However, on slides where large numbers cells were spread randomly throughout the slide, manual analysis of a slides centerline could not accurately predict epithelial cell measurements for the entire slide.

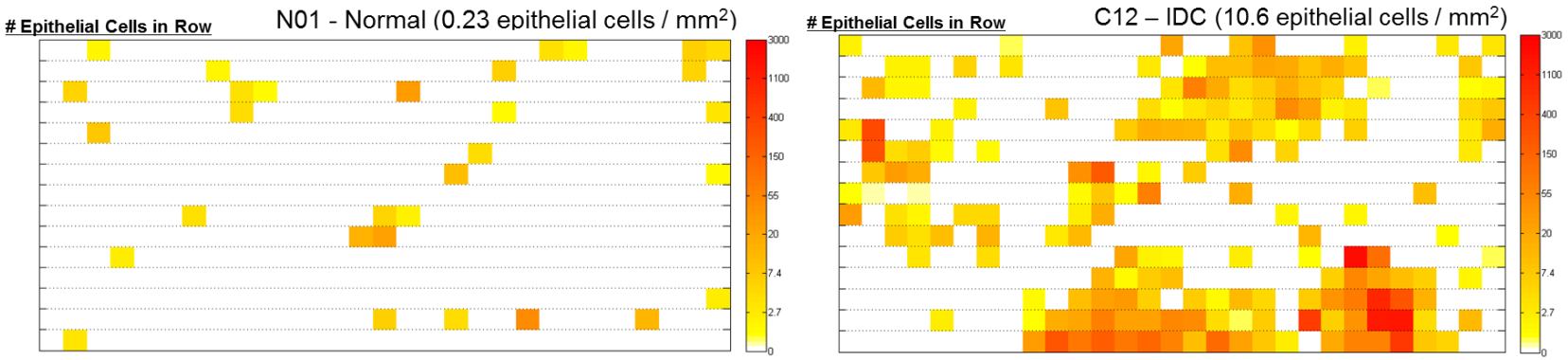

Figure 1.6: Automated Epithelial cell count by image tile row (Top – IDC, Bottom – Normal). These pictures represent the number of epithelial cells in each section of the slide. Areas of red indicate the greatest number of cells while areas of yellow indicate lower numbers of cell in any given image tile. In cases of invasive carcinoma, where many cells are present throughout the slide, manual and automated microscopy provide similar results. In slides with few cells scatter across the slide, such as with normal tissue, manual microscopy will be less accurate as there is a great deal of variation in epithelial cell density depending on which area of the slide is studied.

1.5 - DISCUSSION

Obtaining negative margins during BCT operations remains a vexing problem for surgeons and patients with breast cancer. Imaging techniques, such as mammography, are detecting smaller tumors that are not palpable and are challenging to localize during surgery. Furthermore, many tumors spread along a ductal pattern and even the best imaging techniques may underestimate the amount of disease, particularly for DCIS. Intraoperatively, surgeons must make educated guesses as to the amount of tissue to remove and many times need to perform a second operation to obtain a negative microscopic margin. Furthermore, in patients with lobular cancers, it often is difficult to achieve negative margins because of their diffuse spread [16]. Many techniques have been used to identify positive microscopic margins. Touch/imprint cytology has been utilized since the 1970's to relatively quickly obtain pathological information on fresh specimens without disturbing the tissue for later interpretation. However, an experienced cytopathologist is necessary because correct interpretation can be challenging [18]. The largest series to utilize touch preps for diagnosis and evaluation of surgical margins was completed by Klimberg et al.[11] They studied 428 consecutive patients with breast masses (benign and malignant) and had 83 patients with cancer (74% invasive and 26% DICS). Klimberg et al. performed touch prep on cross-sections to diagnose the lesion and the slides were analyzed by a cytopathologist. In their study the average tumor size was 2.2 cm. This is relatively large and all the specimens were diagnostic excisions (no mastectomies). Therefore, the total volume of tissue removed was lower than in the present study. For the cross-section of the tumor, Klimberg et al. had an accuracy rate of 99% for correctly

diagnosing cancer. Klimberg et al. missed four cancers because of sampling error. At that time, the radiologist used 14 to 18 gauge cores to diagnose breast cancers, so the majority of tumor was still intact at the time of the surgical resection [18].

The incidence of positive margins at University of California, San Diego, is low (10%); [19] therefore, this study utilized cross-sections of freshly excised surgical specimens. However, there were small tumors in the series, which had a high probability of not being sampled. To combat this problem, multiple cuts through surgical specimens were taken. As shown in **Figure 1.3b**, the density of cancer cells varied by approximately 5x, depending on the location of the cross-section cut; the variation may explain some false-negative cases in the cross-section study particularly in specimens of DCIS. To determine the expected accuracy of the tumor detection technique, the probability of missing the tumor in a cross-sectional cut in the absence of palpation was estimated from the size of the tumors and tissue. The average estimated probabilities of missing the tumors are 87.5% for DCIS and 35% for invasive cancer (IDC + ILC; **Table 1.2**). Therefore, the probabilities of detecting the tumors should be 12.5% for DCIS and 65% for IDC + ILC if the cross-section cuts are completely random. These two calculations explain the sampling error observed in this series. At present, radiologists use 9 to 11 gauge core biopsies, which removes a large portion of the tumor [20]; therefore, in the present study, the sampling error is an even larger problem for both manual and automated microscopy to obtain an accurate identification if few cells are present. Therefore, in the reported numbers for sensitivity of the automated cellularity touch prep technique are always reported as

minimum sensitivity because it is hypothesized that some of the negative scores are solely due to the tumor not being sampled.

The objective of this pilot study was to create a system to evaluate surgical margins intraoperatively primarily for patients undergoing breast conservation therapy for the treatment of breast cancer. The data are consistent with the viability of utilizing immunofluorescent staining and automated microscopy to detect cancer cells in touch preps. Confirmatory studies with larger patient populations are required to definitively prove that this automated system is reliable. The biggest challenge to surgeons is obtaining negative margins for patients undergoing breast conservation therapy but this system also may be useful for patients undergoing skin-sparing mastectomy or even nipple-preserving mastectomy where surgical margin and local recurrence is still an issue [21]. Some patients with large palpable tumors or large areas of calcifications were included in this pilot project to maximize the probability of identifying the area of tumor within the breast for analysis. Many of these patients chose to undergo mastectomy because they had large palpable tumors or large areas of calcifications on mammogram. Some of the mastectomy tissue was used as part of the ‘‘normal’’ samples for this study, slightly increasing the difficulty of distinguishing between normal and cancer tissue because the normal tissue was from a high-risk individual with more cellular atypia. Of the 13 mastectomy cases included in this study, 4 mastectomies were prophylactic for high-risk patients (normal control tissue) and 9 mastectomies were performed due to large tumor size, multi-centric disease, previous radiation, or patient preference. The 11 breast conservation cases included smaller tumors. The preliminary results of this evaluation of the automated microscopy system

show that the technique is likely to be successful and could be implemented in any hospital without special expertise in cytopathology to identify cancer cells at surgical margins for invasive breast cancer. Touch prep of the surgical margins, a rapid immunofluorescence staining protocol, and low-resolution automated microscopy can be employed to calculate the number of epithelial cells across the entire slide to differentiate invasive cancer from benign tissue with at least 83% accuracy. Eventually the technique will at least have a comparable processing and analysis time as standard frozen section. It is estimated that with a 14-megapixel camera, the setup time for automatic focus will be less than 1 min and the scanning time for a whole slide will be less than 5 min.

This technique is promising to accurately identify invasive cancer cells and can be translated to evaluate the status of surgical margins. The potential of the technique to reduce re-excision can be estimated assuming that the optimized touch prep procedure would be approximately as efficient on surgical margin as it is on cross-sectional cuts. Most operations involve the use of electric cautery, which may limit the number of evaluable cells on the touch prep slides and increase the cellular fragmentation due to thermal injury. However, other investigators have successfully used hematoxylin and eosin-stained touch prep analysis on cauterized margins and newer technologies to remove breast tumors are being developed that limit thermal injury to cells [11, 22]. In the current small pilot study, the correct identification rates were 100% of ILC cases, 80% of IDC cases, and 40% of DCIS cases; therefore, it is estimated that the positive margin rate will cut in half when utilizing this technique. It is noted that this estimate will be lowered if the touch prep process is less efficient on

heavily cauterized tissue and the estimate will be higher after correcting for sample errors in the DCIS cases. Future studies to improve the accuracy of DCIS diagnosis will focus on using an automated microscopic analysis of the nuclear features of each cell at higher resolution; the work by Klimberg shows that this should identify even DCIS cells. This study paves the way to devise a rapid intraoperative procedure to identify breast cancer cells in excised tissue margins. It is expected that in the future, surgeons can utilize this automated microscopy system and software in the operating room and will be able to more fully evaluate the surgical margins at the time of the patient's initial operation for breast conservation surgery. This technique will reduce the necessity for multiple operations to obtain negative margins in the surgical treatment of breast cancer.

1.6 ACKNOWLEDGEMENTS

Chapter 1, in full, is a reprint of the material as it appears in Annals of Surgical Oncology, vol 16, 2009, Cortes-Mateos, Maria Jose; Martin, David; Sandoval, Sergio; Ruidiaz, Manuel E.; Messmer, Davorka; Wang-Rodriguez, Jessica; Trogler, William; Kummel, Andrew C.; Blair, Sarah L. The dissertation author was the primary investigator and author of this paper.

1.7 REFERENCES

1. Fisher B, Anderson S, Bryant J, et al. Twenty-year follow-up of a randomized trial comparing total mastectomy, lumpectomy, and lumpectomy plus irradiation for the treatment of invasive breast cancer. N Engl J Med. 2002;347:1233–41.

2. Fisher B, Anderson S, Redmond CK, et al. Reanalysis and results after 12 years of follow-up in a randomized clinical trial comparing total mastectomy with lumpectomy with or without irradiation in the treatment of breast cancer. N Engl J Med. 1995;333:1456–61.

3. van Dongen JA, Bartelink H, Fentiman IS, et al. Factors influencing local relapse and survival and results of salvage treatment after breast-conserving therapy in operable breast cancer: EORTC trial 10801, breast conservation compared with mastectomy in TNM stage I and II breast cancer. Eur J Cancer. 1992;28A:801–5.

4. Lichter AS, Lippman ME, Danforth DN Jr, et al. Mastectomy versus breast-conserving therapy in the treatment of stage I and II carcinoma of the breast: a randomized trial at the National Cancer Institute. J Clin Oncol. 1992;10:976–983.

5. Krishnan L, Stanton AL, Collins CA, et al. Form or function? Part 2. Objective cosmetic and functional correlates of quality of life in women treated with breast-conserving surgical procedures and radiotherapy. Cancer. 2001;91:2282–7.

6. Mansfield CM, Komarnicky LT, Schwartz GF, et al. Ten-year results in 1070 patients with stages I and II breast cancer treated by conservative surgery and radiation therapy. Cancer. 1995; 75:2328–36.

7. Mullenix PS, Cuadrado DG, Steele SR, et al. Secondary operations are frequently required to complete the surgical phase of therapy in the era of breast conservation and sentinel lymph node biopsy. Am J Surg. 2004;187:643–6.

8. Meric F, Mirza NQ, Vlastos G, et al. Positive surgical margins and ipsilateral breast tumor recurrence predict disease-specific survival after breast-conserving therapy. Cancer. 2003;97:926–33.

9. Singletary SE. Surgical margins in patients with early-stage breast cancer treated with breast conservation therapy. Am J Surg. 2002;184:383–93.

10. Muttalib M, Tai CC, Briant-Evans T, et al. Intraoperative assessment of excision margins using breast imprint and scrape cytology. Breast. 2005;14:42–50.

11. Klimberg VS, Harms S, Korourian S. Assessing margin status. Surg Oncol. 1999;8:77–84.

12. Creager AJ, Shaw JA, Young PR, et al. Intraoperative evaluation of lumpectomy margins by imprint cytology with histologic correlation: a community hospital experience. Arch Pathol Lab Med. 2002;126:846–8.

13. Otsu N. A threshold selection method from grey level histograms. IEEE Trans Syst Man Cybern. 1979;9:62–6.

14. Canny J. A computational approach to edge detection. IEEE Trans Pattern Anal Mach Intell. 1986;8:679–98.

15. Cooke T, Peake M. The optimal classification using a linear discriminant for two point classes having known mean and covariance. J Multivar Anal. 2002;82:379–94.

16. Dillon MF, Hill AD, Fleming FJ, et al. Identifying patients at risk of compromised margins following breast conservation for lobular carcinoma. Am J Surg. 2006;191:201–5.

17. Gschwind R, Umbricht CB, Torhorst J, Oberholzer M. Evaluation of shape descriptors for the morphometric analysis of cell nuclei. Pathol Res Pract. 1986;181:213–22.

18. Rosenblatt R, Fineberg SA, Sparano JA, et al. Stereotactic core needle biopsy of multiple sites in the breast: efficacy and effect on patient care. Radiology. 1996;201:67–70.

19. Blair SL, Wang-Rodriguez J, Cortes-Mateos MJ, Messmer D, Sandoval S, Messmer B, et al. Enhanced touch preps improve the ease of interpretation of intraoperative breast cancer margins. Am Surg. 2007;73:973–6.

20. Povoski SP, Jimenez RE. A comprehensive evaluation of the 8- gauge vacuum-assisted Mammotome® system for ultrasoundguided diagnostic biopsy and selective excision of breast lesions. World J Surg Oncol. 2007;5:83.

21. Carlson GW, Page A, Johnson E, et al. Local recurrence of ductal carcinoma in situ after skin-sparing mastectomy. J Am Coll Surg. 2007;204:1074–80.

22. Priglinger SG, Palanker D, Alge CS, et al. Pulsed electron avalanche knife: new technology for cataract surgery. Br J Ophthalmol. 2007;91:949–54.

CHAPTER 2

Quantitative Automated Image Analysis System with Automated Debris Filtering for Detection of Breast Carcinoma Cells

2.1 ABSTRACT

Objective: To develop an intraoperative method for margin status evaluation during breast conservation therapy (BCT) using an automated analysis of imprint cytology specimens.

Study Design: Imprint cytology samples were prospectively taken from 47 patients undergoing either BCT or breast reduction surgery. Touch preparations from BCT patients were taken on cut sections through the tumor to generate positive margin controls. For breast reduction patients, slide imprints were taken at cuts through the center of excised tissue. Analysis results from the presented technique were compared against standard pathologic diagnosis. Slides were stained with Cytokeratin and Hoechst, imaged with an automated fluorescent microscope, and analyzed with a fast algorithm to automate discrimination between epithelial cells and non-cellular debris.

Results: Accuracy of the automated analysis was 95% for identifying invasive cancers compared against final pathologic diagnosis. Overall sensitivity was 87% while specificity was 100% (no false positives). This is comparable to the best reported results from manual examination of intraoperative imprint cytology slides while reducing the need for direct input from a cytopathologist.

Conclusion: This work demonstrates a proof of concept for developing a highly accurate and automated system for intraoperative evaluation of margin status to guide surgical decisions and lower positive margin rates.

2.2 INTRODUCTION

Breast conservation therapy (BCT) or partial mastectomy has been proven to have equal survival efficacy compared to full mastectomy through multiple studies with greater than 10 years of follow-up and is currently considered the standard of care [1-4]. Despite advances in pre-operative imaging and tumor localization through ultrasound and MRI, positive margin rates in BCT continue to range from 25-50%; positive margins have negative consequences for patients, surgeons, and the healthcare system, requiring additional treatments to ensure disease free outcomes [5, 6]. Several studies have employed the use of intraoperative frozen section analysis to evaluate the need to excise additional tissue during surgery [7]. However, frozen section analysis is a difficult, time consuming, and tissue destructive procedure that can be impractical for evaluation of an entire lumpectomy surface. Imprint cytology has been shown to have equal accuracy in detecting positive margins compared to frozen section analysis while completely preserving tissue for traditional permanent section analysis [8, 9]. Through the use of skilled cytopathologists, intraoperative imprint cytology has been successfully used in large scale clinical studies to reduce positive margin rates [10-12]. However, the screening by the cytopathologist can be time consuming and could prolong the surgical procedure. A previous related study by Cortes-Mateos et al. used

a semi-automated software-based image analysis of epithelial cell density across an entire slide to validate that the number of epithelial cells sampled by imprint cytology is a good metric for positive margins [13]. The present study describes the first use of a fast, completely automated analysis technique including automated debris filtering and autofocusing (in contrast to the previous study) so that no immediate input is needed by a cytopathologist. Furthermore, in the present study, analysis of permanent sections of tissue local to the region sampled by imprint cytology significantly improved the measures of accuracy and the ability to validate the current technique.

2.3 BACKGROUND

Digital pathology and computer aided diagnosis (CAD) are rapidly growing fields in the medical industry. Several competing companies and research laboratories are developing technology and software application suites that allow researchers and pathologists to analyze, quantify, and diagnose digital image data collected from the numerous imaging modalities, including bright field and fluorescence microscopy, MRI, ultrasound, CT, etc. Most applications utilizing optical microscopy attempt to perform more accurate measurements of cellular features that pathologists typically employ in making a diagnosis. CAD combines multiple quantitative measurements taken from each individual cell and subsequently employs pattern recognition or machine learning algorithms to classify or grade cells. While mimicking standard pathological analyses, CAD can exceed human performance in quantitative measurements such as DNA content or size of organelles within each cell [14-17]. The

majority of CAD tools are powered by supervised classification algorithms which self-adapt to recognize the different classifications of tissue expected within a set of images. These algorithms are first supplied with a training set wherein each cell has been pre-classified by pathologist. Subsequently, algorithm performance is evaluated on an independent test set of images without any pre-classified cells. Problems can arise from imaging or sample preparation artifacts that preclude automated analysis from measuring suitable differences between different classes of cells under investigation. With careful evaluation and interaction with experienced pathologists, these techniques are often quite successful [18-23].

However practical use of supervised classification algorithms can be limited by the computational processing required to classify a large dataset with a selected algorithm [24]. For most tissue section preparations, a bright field stain such as Hematoxylin and Eosin (H&E) is used by pathologists to evaluate tissue architecture and cellular grade to make determinations of disease progression. Selecting the proper measurements to distinguish tissue grades and validating the training set for the problem at hand can take considerable skill and experience [25]. By comparison, performing a fast intraoperative margin status evaluation of a cancerous tumor requires a simple “yes or no” classification; the exact stage of disease progression is less important than knowing if disease is present or absent at the surgical margin. As far as we know, there are no reports of CAD for intraoperative analysis of breast cancer surgical margins. For imprint cytology of breast surgical margins, CAD of individual cells is challenging since most of the cancer cells are present in three

dimensional clusters with unclear boundaries between neighboring and overlapping cells.

In the present study of breast cancer surgical margins, the classification classes for this technique were reduced simply to cancer and non-cancer. In addition, fluorescent imaging and stains were used since highly specific antibody-antigen binding accomplishes the majority of the task of identifying the desired cells in a sample and can detect the cancer cells being in three dimensional clusters. Nevertheless, immunofluorescent staining is not perfect and non-specific binding, environmental debris, and sample preparation can all introduce fluorescent artifacts that would be recognized as cells in any algorithm using only an intensity threshold to classify recognized objects on a slide. For these reasons, a fast algorithm was developed based on simple statistical, correlational, and morphological parameters to distinguish true epithelial cells from other fluorescently labeled debris located on imprint cytology specimens.

2.4 METHODS

2.4.1 Surgical Samples

Institutional Review Board approval from the University of California, San Diego was obtained to study breast cancer and non-cancer tissue from patients. All patients underwent their planned procedure for breast surgical treatment, and the specimens were removed and sent to the pathology laboratory for analysis. As controls, non-cancer samples were acquired from two groups of patients: normal tissue

was collected from patients undergoing breast reduction surgery; prophylactic tissue was obtained from patients undergoing prophylactic mastectomy of a non-cancerous breast. All surgeries were performed at the University of California, San Diego Medical Center. Standard techniques for resection of breast tissue were employed including electric cautery (Valley Labs, Boulder, CO). Fresh specimens were gently imprinted onto poly-L-lysine (PLL) coated glass slides (Newcomer Supply, Middleton, WI).

2.4.2 Touch Preparation for Breast Epithelial Cells

After excision, surgical specimens were grossed by a pathologist. The area with the highest probability of containing tumor cells was located by palpation or by an image guided wire that was placed preoperatively. A cut through the tumor was made at this location to generate a "calibrated" positive margin with an area with high probability of containing tumor cells. As explained below, permanent or frozen section pathology was performed suspicious tissue so to verify that cancer cells were present in the "calibrated" positive margin. For larger tumors, tissue was flash frozen for later analysis and for smaller tumors the area was specially inked for later identification. These calibrated margins represent the worst possible outcome: a slice directly through the tumor with no margin of healthy tissue. Poly-L-lysine (PLL) coated slides were touched on both halves of the exposed tissue in the cross sectional cut in a process known as imprint cytology or touch prep. For the permanent section analysis of this same region of tissue, a planar sample of the tissue was sectioned from the tumor surface for either paraffin embedding in a cassette (for T1 tumors, 2cm or less)

or for frozen sectional analysis in a frozen tissue block (for T2 and T3 tumors, greater than 2cm). In most cases, four imprint cytology slides were available for automated analysis. Two slides were taken directly from the tumor surface, and the retained tissue sample was sandwiched between two additional slides (see **Figure 2.1**). For some small tumors, only three imprint cytology slides were taken due to small amount of tumor available for study.

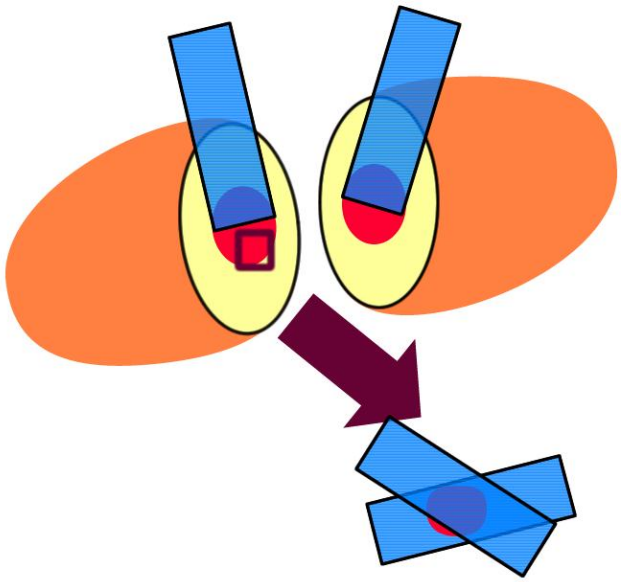

Figure 2.1: Cross sectional slice at the suspected tumor location. Touch preps are taken from both sides of the cut, and a small tissue session from the tumor (red) is excised and saved in a cassette for further analysis (box). One or two touch preps were taken on the excised segment depending on the size of the tissue removed.

To ensure that the automated analysis and the standard pathological analysis were compared on the same location in the surgical specimen in all cases, localized pathological analysis was performed by a board certified pathologist (JWR) to confirm the presence or absence of cancer from the imprint cytology location. Several 5 micron thick microtome sections (up to 12) were made through the tissue sample; to insure the most conservative data analysis, if the pathologist found cancer in any of the sections, the entire tissue sample was declared positive. This local pathology was not performed in the previous study by Cortes-Mateos et al.; therefore the sensitivity was most likely underestimated.

2.4.3 Immunofluorescence Staining and Automated Microscopy

The immunofluorescent staining protocol was previously reported in detail and validated by Cortes-Mateos et al. [13]. Hoechst, a DNA stain was used a nuclei marker, and Cytokeratin was used as an epithelial cell marker. The complete staining protocol, which including fixation, permeabilization, and blocking, required 20-25 minutes. Others have found that immunofluorescence staining protocols can be reduced to only 10 minutes by decreasing fixation time, skipping the blocking step, and decreasing incubation time while maintaining image quality [26]. An automated scanning stage microscope was used for the data acquisition (AxioImager Z1, Carl Zeiss Inc., Thornwood, NY). Automated control of the microscope was handled by a custom software application. The entire surface of each imprint cytology slide was imaged at a magnification of 5x using a 1.4 megapixel camera (Cool-SNAP HQ2, Photometrics, Pleasanton, CA); the imaging resolution was 1.267μm / pixel. Two

fluorescent images (one for Hoechst fluorescence and one for Cytokeratin fluorescence) were recorded at each image tile, and software autofocusing was employed to select the imaging plane [27, 28].

2.4.4 Image Processing

Hoechst and Cytokeratin images were employed to count the number of epithelial cells even when large clusters of epithelial cells were present. If all the epithelial cells were single isolated cells, it would be easy to distinguish the epithelial cells from cytological debris (fragments of fat, necrosis, fibrin, and fragmented cytoplasmic material) based on the characteristic size and shape of epithelial cells. However, the epithelial cells from cancer cases are usually captured in large clusters. Therefore, for the cell counting to be effective, clusters of epithelial cells must be distinguished from cytological debris which was also present on the slide. The method of recognizing epithelial cells began with generating outlines for all fluorescing objects in a given Cytokeratin image. The computed Cytokeratin outlines were mapped to their corresponding Hoechst fluorescence image to obtain additional measurements (**Figure 2.2**). To screen true epithelial cell outlines from outlines of cytological debris, a simple intensity cutoff for the Hoechst fluorescence was employed. Additional metrics were computed from the Hoechst fluorescence values and used to identify non-cellular debris as explained in the debris filtering section.

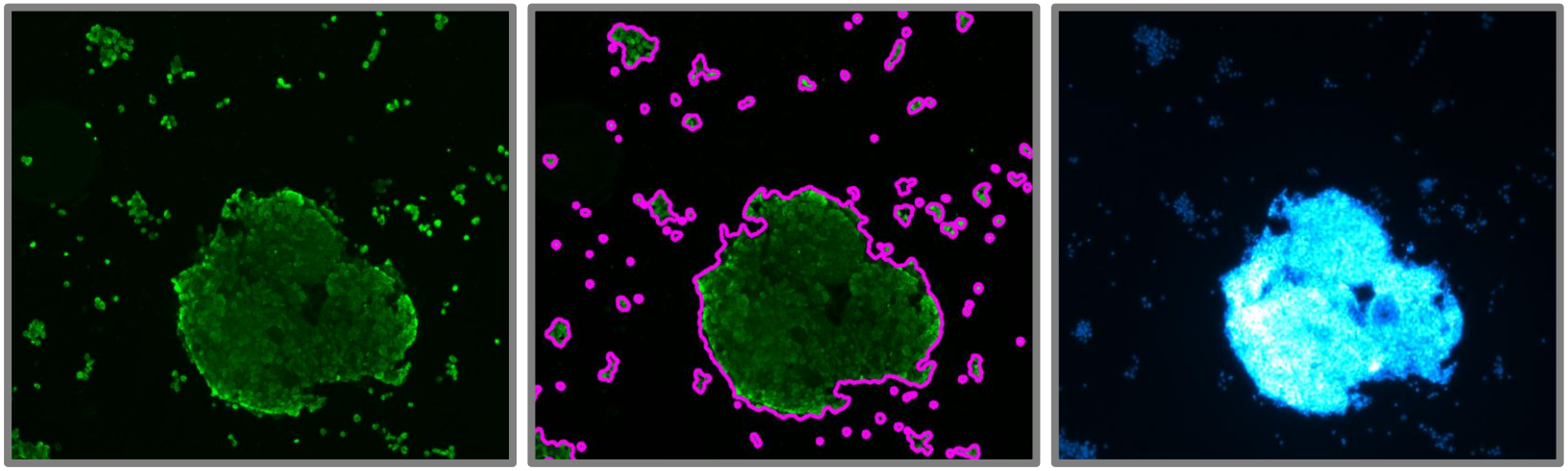

Figure 2.2: Cellular outlining from cytokeratin. A large epithelial cell cluster is surrounded by several smaller clusters and individual cells. The image of raw Cytokeratin fluorescence, from positively stained epithelial cells (left), is used as an input to the software outlining algorithm. Outline results are drawn in pink around recognized cells and clusters, and are subsequently measured for size and location (middle). The Hoechst fluorescent image is used to aid in discriminating real cells from debris (right).

The outlining process for Cytokeratin images was as follows: the image was background subtracted to eliminate any intensity offsets. Subsequently, the image was converted into a binary image using Renyi entropy thresholding, which was selected for its robustness in determining proper threshold values across a variety of images [29]. Median filtering was applied to the binary image to remove any single pixel noise [30, 31]. Two binary morphological operators were applied to the image in order to connect disjoint sets of pixels: a binary closure and a binary opening [32]. Finally a connected component algorithm, wherein adjacent white pixels were grouped together to create a set of boundary pixels, was applied to obtain outlines of objects in the binary image [33]. The pixel coordinates of each outline were mapped back to the original image for the calculation of cellularity metrics to distinguish epithelial cells and cell clusters from debris.

2.4.5 Debris Filtering

Fibers, dust, cellular fragments, and non-specific staining, hereafter collectively referred to as “debris”, can all fluoresce as brightly as stained cells in fluorescence imaging; consequently the debris will also be outlined by the above steps and cannot be distinguished from true epithelial cells by a simple intensity cutoff. In the previous study by Cortes-Mateos et al., this issue was overcome by manually removing image tiles with significant debris from the image set prior to analysis. For the current study, a method of automatically rejecting non-cellular outlines based on quantitative metrics was developed. After the initial outlining process was performed

on an image, candidate outlines were screened on an individual basis by four different debris filters based on properties of the fluorescence intensity distribution:

(1) Hoechst and Cytokeratin each exclusively stain different regions of the cell: the nucleus and the cytoplasm, respectively; therefore, the features of an epithelial cell or cell cluster appear significantly different in each channel. In contrast, fibers, dust, and some nonspecific staining in a fluorescence image tend to look highly similar in both the Hoechst and Cytokeratin channels. If the coefficient of variance of the Cytokeratin and Hoechst fluorescence of an outline were within 5% of each other, the outline was rejected (**Figure 2.3a,b**).

(2) An additional filter was employed to take advantage of the achromaticity of fiber and dust. If the correlation coefficient of the Cytokeratin and Hoechst fluorescence was 0.75 or greater, the outline was rejected; an example is shown in **Figure 2.3c,d**.

(3) Another filter was established which eliminates outlines of debris with a lack of features in either channel. For example, non-specific staining can sometimes be seen as large pools of dye in a fluorescence image with a relatively flat intensity distribution. If either the Cytokeratin or the Hoechst percent standard deviation was 25% or less, the outline was rejected; an example is shown in **Figure 3e,f**.

(4) Air bubbles created during the immunofluorescent staining process have a tendency to collect unbound stain at their borders, causing their edges to fluoresce brightly during imaging (bottom-left of **Figure 2.3a**). Outlines of these bubble edges sometimes included a number of epithelial cells, allowing them to pass the above filters (**Figure 2.3g,h**). However, the characteristic long and narrow shape of these outlines can be detected by measuring its circularity. Circularity is a ratio of the area of the shape to the area of a circle with the same perimeter; long, narrow shapes have low circularity. Outlines of this type of debris were screened out by rejecting all outlines with a circularity value less than 0.2.

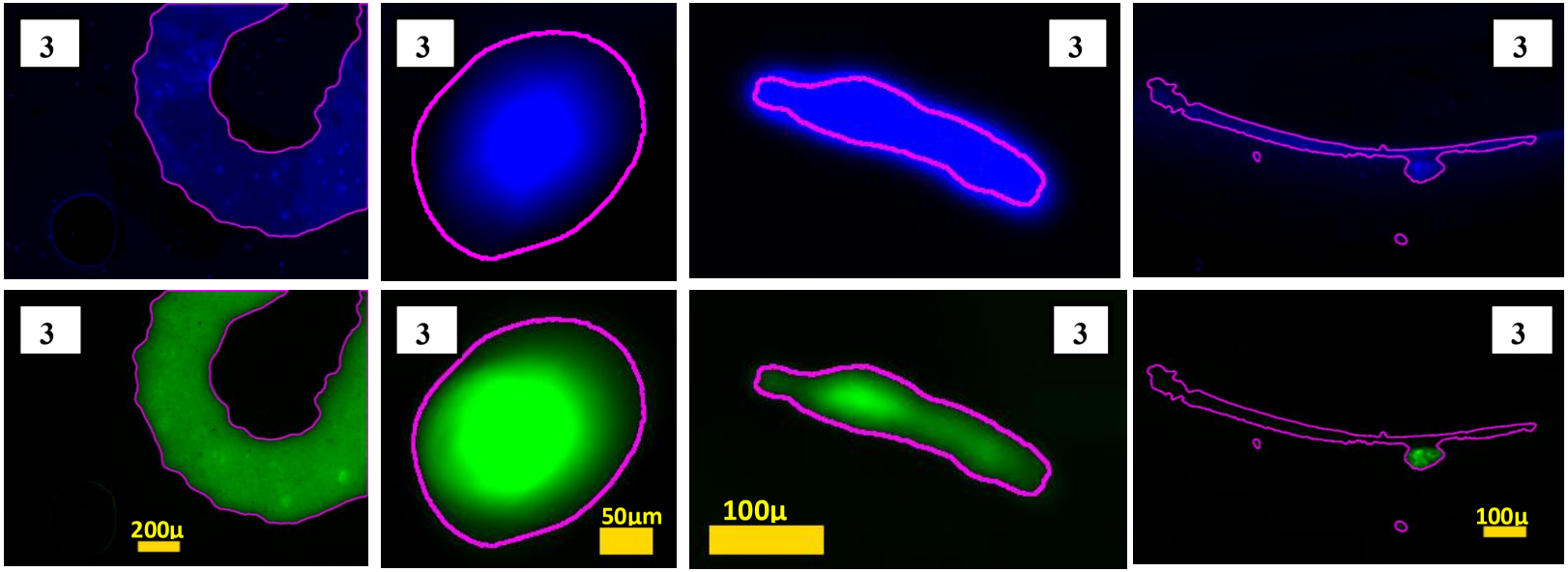

Figure 2.3: Examples of non-cellular debris screened by filters.
(Top Row: Hoechst images, Bottom Row: Cytokeratin images)
2.3a-b): Large area of non-specific staining containing nuclei. Standard deviation refers to staining intensity of Hoechst & Cytokeratin within an outline. Cytokeratin standard deviation = 26.18%, Hoechst standard deviation 26.35%. This feature is classified as debris since standard deviations of the two channels are within 5%.
2.3c-d): A piece of dust fluorescing similarly in both channels. With a Cytokeratin & Hoechst correlation coefficient of 0.896, the piece of dust is determined to be non-cellular.
2.3e-f): A fiber with highly uniform fluorescence. The Hoechst standard deviation is 10.36%, exhibiting hardly any variability across the feature.
2.3g-h): Cells near the edge of a large air bubble generate an outline with a large amount of empty space. A circularity of 0.06 indicates that the outline is erroneous.

Using an independent test set of slides, cutoff values for the filters were determined by manually measuring the properties of a large number of debris outlines, and choosing values to screen out the large majority of debris while minimizing the removal of valid cellular outlines. Identical cutoff values were employed for all slides that were studied. With a larger patient study, establishing a classified training set with machine learning algorithms or neural networks would further optimize the effectiveness of these debris filters.

2.4.6 Epithelial Cell Density

The epithelial cells from positive margins often appeared on the imprint cytology slides in dense clusters. Multilayer cell clusters and cell overlap make it difficult to obtain outlines of individual epithelial cells within a dense cluster. This overlapping of cells was not a critical issue in this study since the presence of a large cluster of epithelial cells was a very strong indicator of the presence of cancer in the margin. The number of epithelial cells in the epithelial cell cluster was calculated by dividing the area of an outline of the entire Cytokeratin positive cluster by 200 μm2, the estimated average area of a single epithelial cell. This method assumes that all clusters occupy a two-dimensional plane, thereby undercounting the number of epithelial cells in multilayered clusters. Since the same estimated epithelial cell area was used for all cases, the actual value used was irrelevant when comparing cellular density. Cellular density for a slide was determined by dividing the total number of epithelial cells by the scanned area of the slide. For all surgical cases, the slide with the highest determined density is reported.

2.5 RESULTS

2.5.1 Debris Filtering

Automated debris filtering was qualified on an independent test set of patient slides from a previous study where manual removal of debris had been employed. The test set consisted of slide images from 24 cancer patients and 10 non-cancer patients: 34 in total [13]. The image processing algorithm described above was employed to identify potential cells and cell clusters. Manual average epithelial cell density for a given slide was calculated after visually inspecting and manually removing images containing debris outlines from the density calculation. Automated average epithelial cell density was calculated by establishing cutoff values for the filtering metrics. After optimization of debris filter cutoff values, strong correlation between manual and automated filtered epithelial cell density was achieved over 4 orders of magnitude in the test set of slides. The optimized cutoff values were used for debris filtering with patient slides discussed in this paper (**Figure 2.4**). The correlation coefficient between the manual and automated filtering was 0.93 over 4 orders of magnitude in cell density, and the slope of the regression line was near unity. This suggests that the cellular counts with the automated debris filtering are nearly equivalent to that of the manually filtered image set. A regression line with slope greater than or less than unity would indicate over-filtering or under-filtering, respectively. The few outliers that deviate from the regression line are sampled across different diagnoses, signifying that the automated debris filtering is equally effective across all types of cases.

Additionally, automated filtering removes individual outlines of debris within an image, rather than removing an entire image from the dataset as was done during manual filtering. This should improve the accuracy of cellular detection, particularly for slides with a low cellular density.

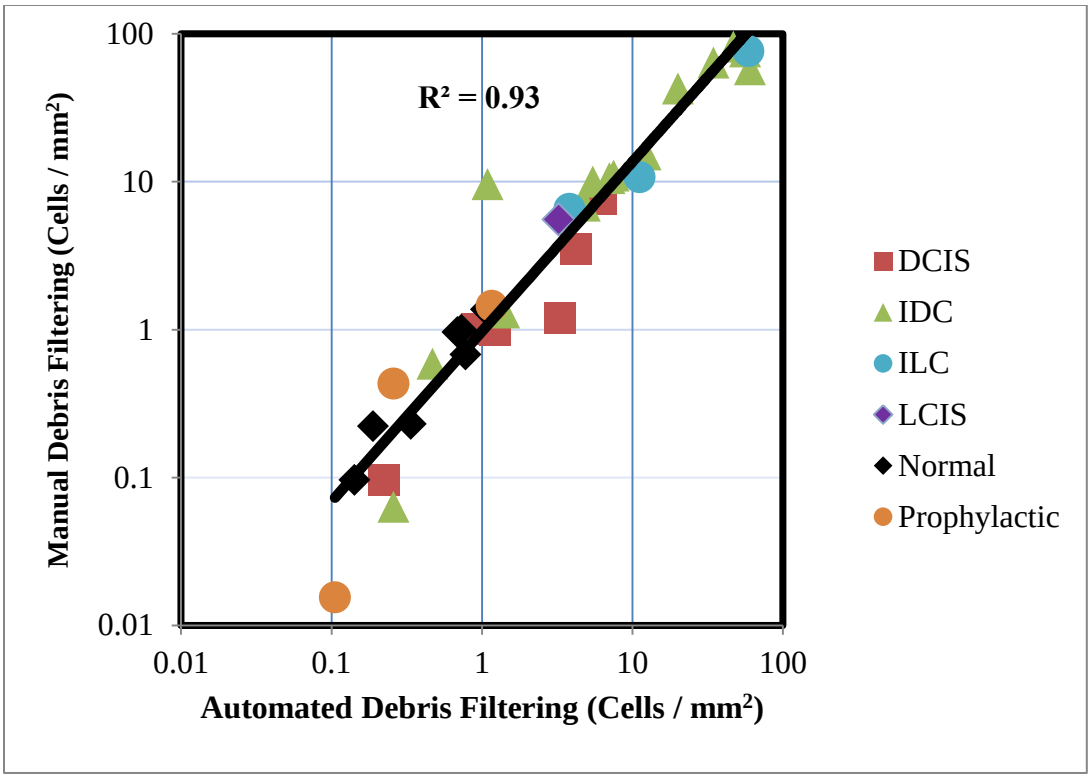

Figure 2.4: Manual vs. Automated Debris Filtering. Automated debris filters were tested against manual removal of debris on a dataset encompassing a mixture of cancer and non-cancer patients (n=34). Automated filtering matched the results of manual filtering with a high correlation (0.93).

The cellular densities of slides were compared before and after debris filtering. As shown in **Figure 2.5** for prophylactic and normal cases, the debris filtering reduced apparent cell density by up to a factor of 25. Several of the imprint cytology slides

from normal and prophylactic patients contained large amounts of debris; if no debris filtering were employed, these slides would appear to have as high a cellular density as cancerous cases. After debris filtering, the average number of epithelial cells for non-cancer (normal and prophylactic tissue) and negative cancer cases dropped by over an order of magnitude (9.18 epithelial cells / mm^2 vs. 0.667 epithelial cells / mm^2) whereas the average for positive cancer cases dropped by less than a factor of 2 (34 epithelial cells / mm2 vs. 13.2 epithelial cells / mm^2).

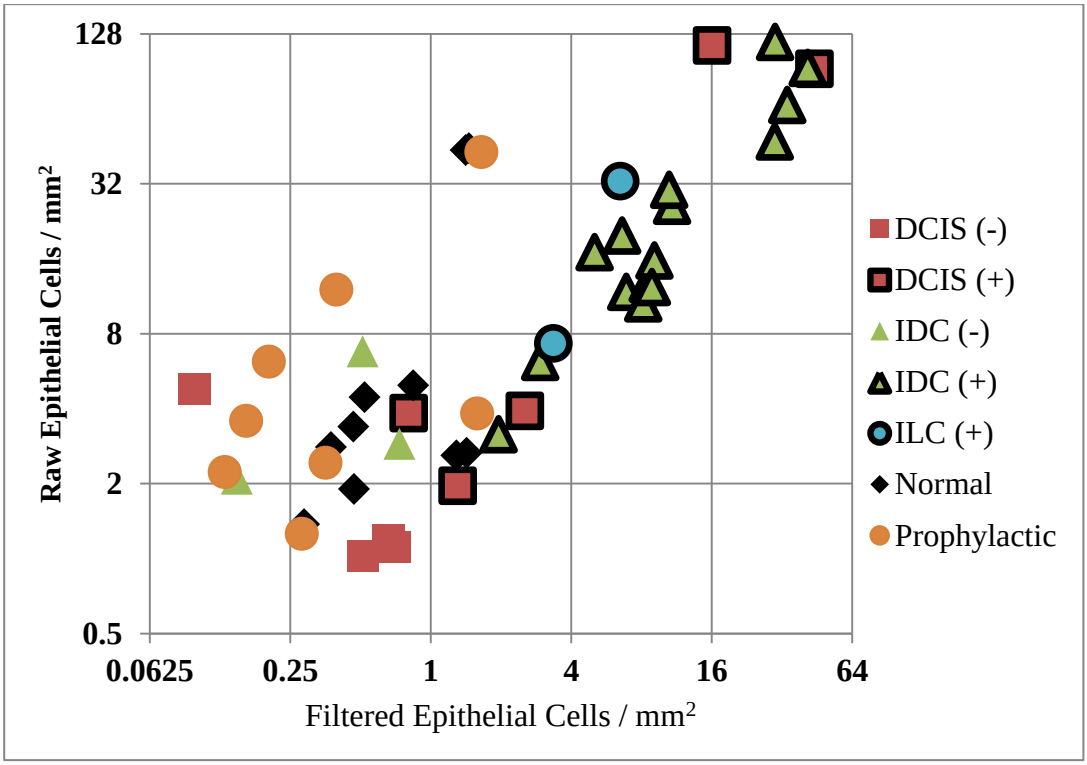

Figure 2.5: Cellular densities before and after debris filtering. Cellular density was compared before (Raw Epithelial Cells / mm^2) and after (Filtered Epithelial Cells / mm^2) automated debris filtering. For most cancer cases, debris filtering had a relatively small impact on cellularity while up to a 25x decrease was observed for non-cancer cases. Several normal and prophylactic cases were found to have large amounts of dust, fibers, and non-specific staining which resulted in high cellularity measurements before filtering. Automated filtering of image outlines eliminates false positives from non-cellular debris on touch prep slides.

Typically, filtering had a small impact on the cellular distributions of positive invasive cancer cases while clearly eliminating areas with high debris on prophylactic and normal cases. Cellular density before and after filtering for a representative prophylactic case and a representative IDC case are plotted in **Figure 2.6**. For the prophylactic case, debris filtering most prominently removed areas along the edge of the slide where air bubbles trapped between the slide and coverslip along with non-specific staining generated a large number of erroneous outlines. Manual inspection of the slide verified that the vast majority of erroneous outlines were screened out by the debris filters. For the IDC cases, debris filtering removed approximately half the initial outlined area, but the overall distribution of cells on the slide remained unchanged. While some weakly stained or poorly focused cells may be eliminated by debris filtering, the overwhelming bias against non-cellular artifacts greatly enhances analysis results.

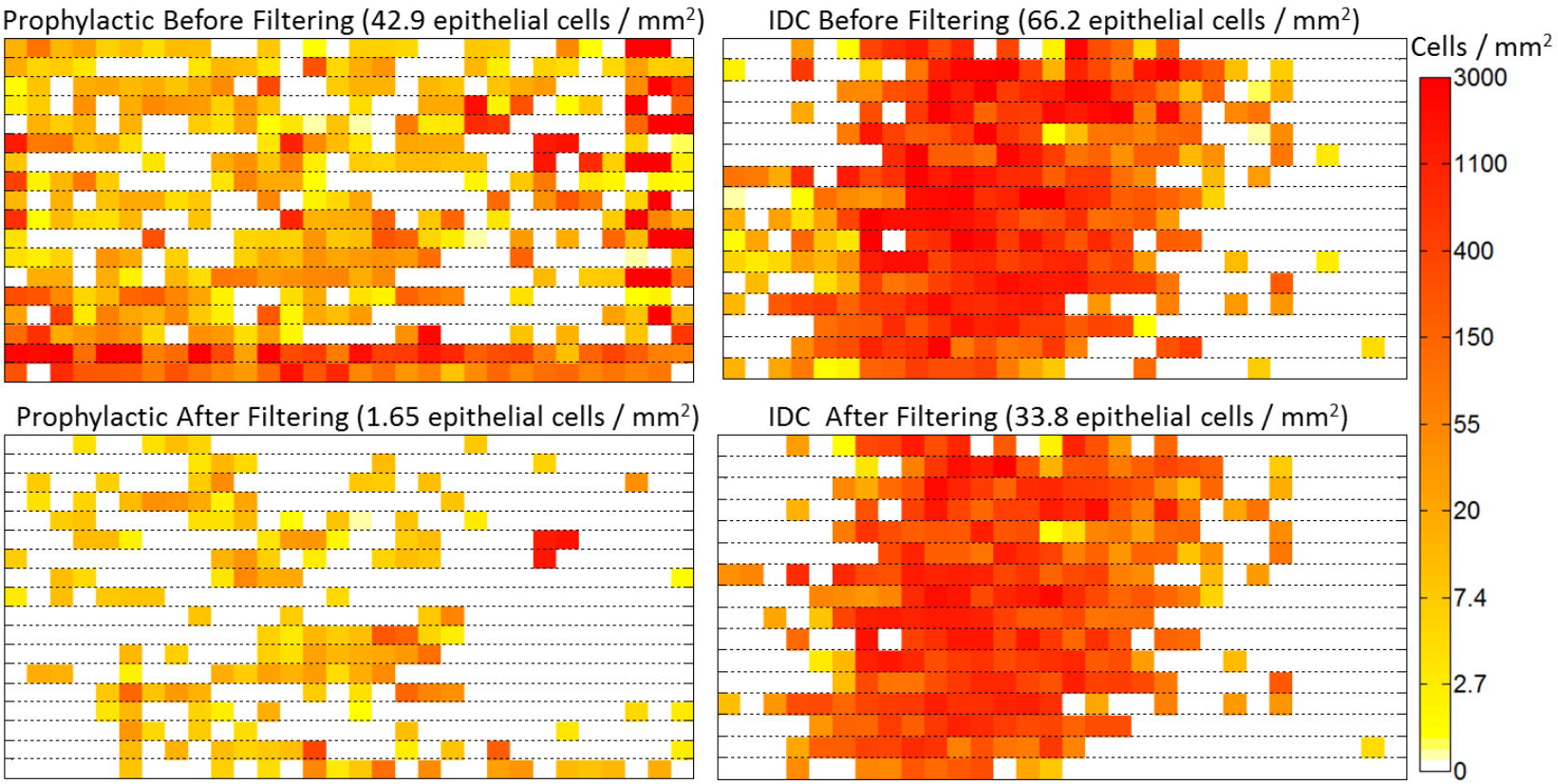

Figure 2.6: Cellular Distributions for Prophylactic and IDC Samples before and after debris removal. The effect of debris filtering was investigated by plotting the cellular density of each image taken of a touch prep slide. (Top left) A typical prophylactic case would be expected to show a low cellularity; however, initial outlines indicate a falsely high cellular density along the edges of the slide. (Bottom left) After debris filtering is performed, debris outlines along the edge of the slide were properly removed, resulting in a 25x reduction in overall cellularity. (Top right) A typical IDC case showed highly dense clusters of cells in the middle of the slide. (Bottom right) After debris

2.5.2 Epithelial Cell Density

For cancer cases, each case was determined to be either positive or negative based upon analysis by a pathologist. All prophylactic and breast reduction cases were considered to be part of the negative population. On average, the positive cancer cases were found to have 13.15 epithelial cells / mm^2 while the negative cases only had 0.6677 epithelial cells / mm^2 with standard deviations of 13.4 (101.9%) and 0.5 (74.97%) respectively. The high degree of variability in the measurement of epithelial cell density made it unlikely to be a robust differentiator between positive and negative cases; however a two sided t-test for unequal variances showed a significant difference between the two populations with $p < 0.01$.

2.5.3 Fractional Coverage

In order to increase the robustness of separating non-cancer and negative cancer cases from positive cancer cases, an additional metric was calculated. Cancer cases exhibit a high density of epithelial cells across large fractions of an imprint cytology slide surface; **Figure 2.6** shows a representative IDC case where nearly half of the slide has a high density of epithelial cells. In contrast, non-cancer cases show only a few small regions with epithelial cells. The few epithelial cells present in benign cases reflect either capture of epithelial cells from a duct ruptured in surgery or possibly some debris missed by filtering. To capture this two dimensional characteristic of the distribution of the epithelial cell density, several scalar metrics were tested. Calculating the percentage of images with a cellular density of at least 5 epithelial cells / mm2 provided the best scalar quantification of cellular distribution

across a whole slide. This distribution metric was found to be 35.9% on average for positive cancer cases, and 4.21% on average for non-cancer and negative cancer cases with standard deviations of 0.168 (46.7%) and 0.0324 (76.9%) respectively. A two sided t-test for unequal variances was performed with $p < 0.001$, revealing a highly significant difference between the positive and negative groups.

While neither metric on its own provides a perfect separation between the positive invasive cancers and non-cancer and negative cancer populations, plotting both on a 2D graph (**Figure 2.7**) shows a high degree of separation. Using discriminant analysis, an optimally separating cutoff line can be drawn between the two populations [34].

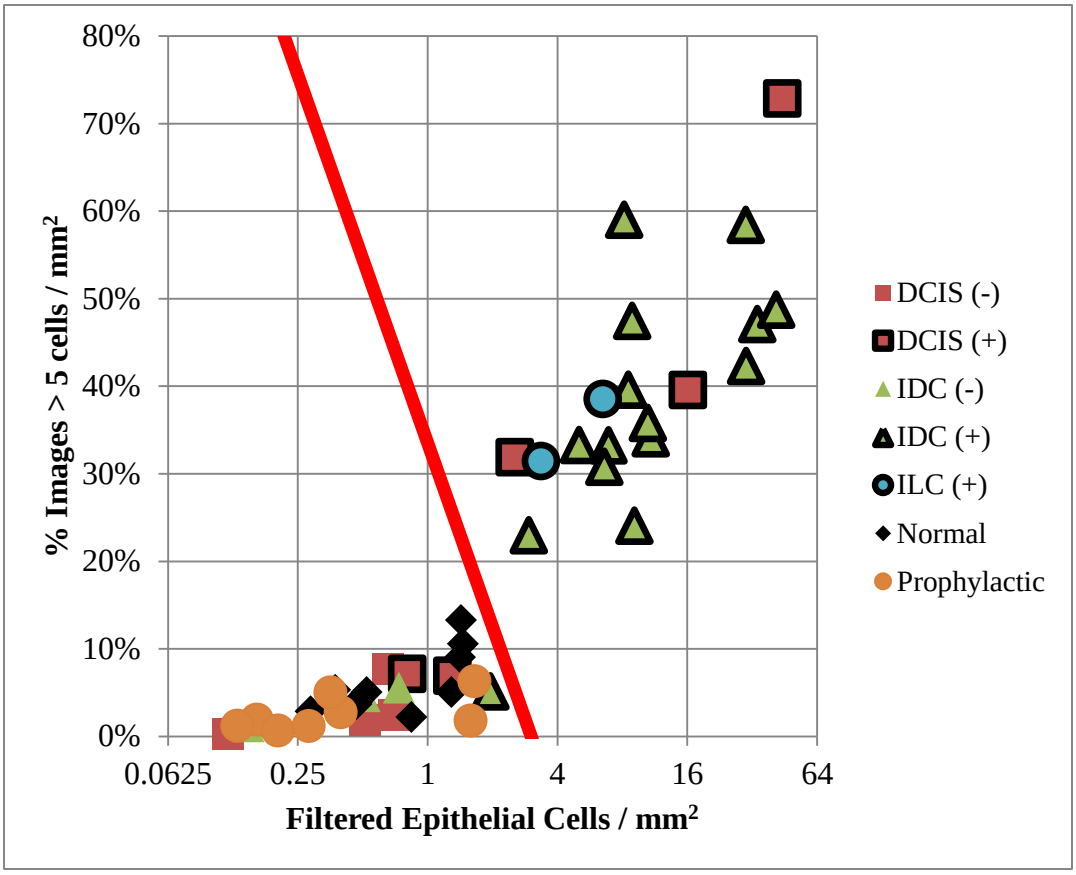

Figure 2.7: Two-dimensional discrimination for cancer detection. % Images > 5 cells / mm^2 vs. filtered epithelial cells / mm^2 .Using two measurements produces a clear separation between positive cancer cases (data points with black outlines) and non-cancer and negative cancer cases (normal, prophylactic, and non-outlined data points); note zero false positives and only 3 false negatives were observed. False negatives are black outlined symbols below the cutoff line.

Sensitivity, specificity, and accuracy results of the automated analysis are tabulated in **Table 2.1**. Specificity was 100% in all tissue types as no false positives were detected. Invasive cancers including invasive lobular carcinoma and invasive ductal carcinoma (ILC + IDC, n = 20) were properly classified with a high degree of accuracy (94.4%) with a single case of IDC reported as a false negative. For the

reported false negative IDC case, local pathological evaluation revealed IDC was present in only 1% of the frozen tissue section slide with a single cluster of cancer cells approximately 100 microns in length. Two cases of ductal carcinoma in situ (DCIS, n = 9) were reported as false negatives. In both of these cases, the pathologist found only a single focus of low grade DCIS. The cellular density of all false negative cases was too low to distinguish them from non-cancer cases. Manual inspection of the slides for these cases confirmed that the slides contained very few epithelial cells, thus indicating a limitation of using epithelial cell counts as a marker for positive margins.

Table 2.1: Summary of Results. Sensitivity, specificity, and accuracy were calculated for all diagnosis types. A cancer case was counted as positive (+) if a pathologist found any cancer in any frozen section or tissue cassette slides. Cancer cases were counted as negative (-) otherwise. No false positives were observed in either cancer or non-cancer patients. Automated analysis reported 3 false negatives across all cancer cases. For each false negative, pathology found cancer in only a single focii, which the presented technique, reliant upon high cellularity in detection, was insensitive to.

Type	Count (-/+)	False Positives	False Negatives	Sensitivity	Specificity	Accuracy
IDC	18 (3/15)	0	1	93.8%	100%	94.4%
ILC	2 (0/2)	0	0	100%	100%	100%
Invasive (IDC+ILC)	20 (3/17)	0	1	94.4%	100%	95%
DCIS	9 (4/5)	0	2	71.4%	100%	77.8%
All Cancer	29 (7/22)	0	3	85%	100%	89.7%
Normal	10 (10/0)	0	0	100%	100%	100%
Prophylactic	8 (8/0)	0	0	100%	100%	100%
Non-Cancer (Normal + Prophylactic)	18 (18/0)	0	0	100%	100%	100%
Cancer + Non-Cancer	47	0	3	88%	100%	93.6%

2.6 DISCUSSION

Compared to previous results from Cortes-Mateos et al., the accuracy of invasive cancer detection (IDC + ILC) by automated detection with debris filtering and locally calibrated samples has increased from 80% to 95% and accuracy of DCIS has increased from 40% to 77.8% across a similar patient population [13]. The increase in accuracy was achieved through the implementation of debris filtering in conjunction with establishing a highly localized pathological review. In particular, the automated debris filtering made a significant contribution in the achievement of 100% specificity. Several would-be false-positive normal and prophylactic cases saw a significant reduction in the overall cellular density measurement (**Figure 2.7**). Relative to Cortes-Mateos et al., the establishment of local pathological analysis helped improve the sensitivity measures and validation of the technique. Since permanent section analysis was not performed on the tissue immediately being sampled by imprint cytology in the previous study, it is likely that many of the imprint cytology samples did not actually sample cancerous tissue, thus overestimating the figures for false-negatives.

The major source of error in this study was likely due to the difficulty of orienting imprint slides on the cross sections of small tumors where the foci of cancer were sometimes as small as a few hundred microns. For very small tumors inside large cross sectional tissue samples, cancer only occupied a small portion of the cross sectional tissue surface; it is likely that the cancer was subsequently missed during imprint cytology. Therefore, it is possible for very small tumors that the pathologist

found cancer in parts of the cross sectional tissue sample which were not sampled by any imprint cytology slides.

These findings are consistent with previous studies using bright-field stains for manual intraoperative analysis of breast cancer surgical margins even though these studies relied upon the expertise of cytologists, including manual analysis of cellular architecture and nuclear characteristics. Cox et al. reported an accuracy of 97.3% in manually assessing margin status across 162 cases [35]. Klimberg et al. reported a manual accuracy of 99.3% across 428 patients [36]. However, England et al. [37] and Saarela et al. [38] reported lower manually accuracies of 73% and 78% respectively. With cytological evaluation experience being the likely differentiator in diagnostic success [8], the use of an automated analysis technique could further the ability to use imprint cytology intraoperatively in areas where expertise is unavailable.

The measurement of nuclear characteristics has long been used in automated analysis of H&E stained slides to differentiate between cancer and non-cancer [39, 40]. A similar approach is being tested to determine if using Hoechst dye could supplement the cellular density measurements to increase accuracy for DCIS. In practice, the presented automated technique could be used intraoperatively to reduce the need for secondary surgeries. The initial preparation and scanning of the slides do not require the presence of a cytopathologist, and if necessary, a pathologist could remotely review and confirm findings from the digital analysis.

Given that the overall automated analysis technique presented here is targeted towards intraoperative analysis, acquisition time is a critical factor for feasibility. Currently, a typical slide requires 0.5 hours to image, including setup time and 5x

(1.267um/pixel) scans. Scanning time can be significantly reduced by coupling a high resolution camera with lower magnification objectives to reduce the number of images required to scan the same area. With a 16 megapixel camera, it is estimated that the total scanning time can be reduced to 10 minutes for the 1.267um/pixel imaging resolution. With a higher speed imaging, the imaging time will be the time limiting factor. Recent work by Iwamoto et al has shown that the antibody staining time can be reduced to 10 minutes. This is competitive with the time required for intraoperative frozen section analysis.

2.7 CONCLUSION

This automated system in conjunction with intraoperative cytological imprints is a highly sensitive and specific method for identification of breast cancer. Because of its rapid turnaround time, this method could in the future be applied to imprints of surgical margins and identification of close or positive margins. The preliminary information would assist in additional tissue removal, if necessary, and significantly reduce the need to perform a second operation at a later time due to positive margins in the final pathology report. The lack of any false positives across the studied patient population is highly encouraging as usage of this technique should not lead to unnecessary removal of extra tissue or cause unnecessary cosmetic deformity. Additionally the non-destructive nature of imprint cytology preserves tissue for traditional permanent section analysis, ensuring a safety net for any false negatives. Use of the automated microscopy technique would ultimately decrease positive

margins rates and the need for second operations in the treatment of early stage breast cancer. This process would entail coordination between the surgeon and pathologist to confirm the automated results and make sure proper sampling of the tumor surface was performed.

2.8 ACKNOWLEDGEMENTS

Chapter 2, in full, is a reprint of the material as it appears in Acta Cytologica, vol. 55, 2011, Martin, David T.; Sandoval, Sergio; Ta, Casey N.; Ruidiaz, Manuel E.; Cortes-Mateos, Maria Jose; Messmer, Davorka; Kummel, Andrew C.; Blair, Sarah L.; Wang-Rodriguez, Jessica. The dissertation author was the primary researcher and author of this paper.

2.9 REFERENCES

1. Lichter, A.S., et al., Mastectomy versus breast-conserving therapy in the treatment of stage I and II carcinoma of the breast: a randomized trial at the National Cancer Institute. J Clin Oncol, 1992. 10(6): p. 976-983.

2. Fisher, B., et al., Twenty-Year Follow-up of a Randomized Trial Comparing Total Mastectomy, Lumpectomy, and Lumpectomy plus Irradiation for the Treatment of Invasive Breast Cancer. N Engl J Med, 2002. 347(16): p. 1233-1241.

3. Fisher, B., et al., Reanalysis and Results after 12 Years of Follow-Up in a Randomized Clinical Trial Comparing Total Mastectomy with Lumpectomy with or without Irradiation in the Treatment of Breast Cancer. N Engl J Med, 1995. 333(22): p. 1456-1461.

4. Carl, M.M., et al., Ten-year results in 1070 patients with stages I and II breast cancer treated by conservative surgery and radiation therapy. Cancer, 1995. 75(9): p. 2328-2336.

5. Funda, M., et al., Positive surgical margins and ipsilateral breast tumor recurrence predict disease-specific survival after breast-conserving therapy. Cancer, 2003. 97(4): p. 926-933.

6. Smitt, M.C. and K. Horst, Association of Clinical and Pathologic Variables with Lumpectomy Surgical Margin Status after Preoperative Diagnosis or Excisional Biopsy of Invasive Breast Cancer. Ann Surg Oncol, 2007. 14(3): p. 1040-1044.

7. Olson, T., et al., Frozen Section Analysis for Intraoperative Margin Assessment During Breast-Conserving Surgery Results in Low Rates of Re-excision and Local Recurrence. Annals of Surgical Oncology, 2007. 14(10): p. 2953-2960.

8. Creager, Intraoperative evaluation of lumpectomy margins by imprint cytology with histologic correlation. Archives of Pathology Laboratory Medicine, 2002. 126(7): p. 846-846.

9. Muttalib, M., et al., Intra-operative assessment of excision margins using breast imprint and scrape cytology. The Breast, 2005. 14(1): p. 42-50.

10. D'Halluin, F.o., et al., Intra-operative touch preparation cytology following lumpectomy for breast cancer: A series of 400 procedures. The Breast. In Press, Corrected Proof.

11. Cox, C., et al., Cytologic evaluation of lumpectomy margins in patients with ductal carcinoma in situ: Clinical outcome. Annals of Surgical Oncology, 1997. 4(8): p. 644-649.

12. Klimberg, V., S. Harms, and S. Korourian, Assessing margin status. Surgical Oncology, 1999. 8(2): p. 77-84.

13. Cortes-Mateos, M., et al., Automated Microscopy to Evaluate Surgical Specimens Via Touch Prep in Breast Cancer. Annals of Surgical Oncology, 2009. 16(3): p. 709-720.

14. Anagnostopoulos, I. and I. Maglogiannis, Neural network-based diagnostic and prognostic estimations in breast cancer microscopic instances. Med Biol Eng Comput, 2006. 44(9): p. 773-84.

15. Boland, M.V., M.K. Markey, and R.F. Murphy, Automated recognition of patterns characteristic of subcellular structures in fluorescence microscopy images. Cytometry, 1998. 33(3): p. 366-75.

16. Chen, W., et al., Image mining for investigative pathology using optimized feature extraction and data fusion. Comput Methods Programs Biomed, 2005. 79(1): p. 59-72.

17. Mattie, M.E., et al., PathMaster: content-based cell image retrieval using automated feature extraction. J Am Med Inform Assoc, 2000. 7(4): p. 404-15.

18. Glotsos, D., et al., Automated diagnosis of brain tumours astrocytomas using Probabilistic Neural Network clustering and Support Vector Machines. International Journal of Neural Systems, 2005. 15(1-2): p. 1-11.

19. Lisboa, P.J. and A.F.G. Taktak, The use of artificial neural networks in decision support in cancer: A systematic review. Neural Networks, 2006. 19(4): p. 408-415.

20. Maglogiannis, I., E. Zafiropoulos, and I. Anagnostopoulos, An intelligent system for automated breast cancer diagnosis and prognosis using SVM based classifiers. Applied Intelligence, 2009. 30(1): p. 24-36.

21. Mango, L.J., Computer-assisted cervical cancer screening using neural networks. Cancer Lett, 1994. 77(2-3): p. 155-62.

22. Zhou, Z.H., et al., Lung cancer cell identification based on artificial neural network ensembles. Artificial Intelligence in Medicine, 2002. 24(1): p. 25-36.

23. Krishnan, M.M.R., et al., Statistical analysis of mammographic features and its classification using support vector machine. Expert Systems with Applications, 2010. 37(1): p. 470-478.

24. Llorà, X., A. Priya, and R. Bhargava, Observer-invariant histopathology using genetics-based machine learning. Natural Computing, 2009. 8(1): p. 101-120.

25. Carpenter, A., et al., CellProfiler: image analysis software for identifying and quantifying cell phenotypes. Genome Biology, 2006. 7(10): p. R100.

26. Iwamoto, S., et al., The application of direct immunofluorescence to intraoperative neurosurgical diagnosis. Biomolecular Engineering, 2000. 17(1): p. 17-22.

27. Price, Comparison of phase-contrast and fluorescence digital autofocus for scanning microscopy. Cytometry, 1994. 16(4): p. 283-283.

28. Shen, F., L. Hodgson, and K. Hahn, Digital Autofocus Methods for Automated Microscopy, I. James, Editor. 2006, Academic Press. p. 620-632.

29. Sahoo, P., C. Wilkins, and J. Yeager, Threshold selection using Renyi's entropy. Pattern Recognition, 1997. 30(1): p. 71-84.

30. Nodes, T. and N. Gallagher, Median filters: Some modifications and their properties. Acoustics, Speech and Signal Processing, IEEE Transactions on, 1982. 30(5): p. 739-746.

31. Weiss, B., Fast median and bilateral filtering. ACM Trans. Graph., 2006. 25(3): p. 519-526.

32. Haralick, Image analysis using mathematical morphology. IEEE Transactions on Pattern Analysis and Machine Intelligence, 1987. 9(4): p. 532-532.

33. Samet, H. and M. Tamminen, Efficient component labeling of images of arbitrary dimension represented by linear bintrees. IEEE Transactions on Pattern Analysis and Machine Intelligence, 1988. 10(4): p. 579-586.

34. Cooke, T. and M. Peake, The Optimal Classification Using a Linear Discriminant for Two Point Classes Having Known Mean and Covariance. Journal of Multivariate Analysis, 2002. 82(2): p. 379-394.

35. Cox, C.E., et al., Touch Preparation Cytology of Breast Lumpectomy Margins With Histologic Correlation. Arch Surg, 1991. 126(4): p. 490-493.

36. Klimberg, V.S., K.C. Westbrook, and S. Korourian, Use of touch preps for diagnosis and evaluation of surgical margins in breast cancer. Annals of Surgical Oncology, 1998. 5(3): p. 220-226.

37. England, D.W., et al., Assessment of excision margins following wide local excision for breast carcinoma using specimen scrape cytology and tumour bed biopsy. European Journal of Surgical Oncology, 1994. 20(4): p. 425-9.

38. Saarela, A.O., et al., Determinants of positive histologic margins and residual tumor after lumpectomy for early breast cancer: A prospective study with special reference to touch preparation cytology. Journal of Surgical Oncology, 1997. 66(4): p. 248-253.

39. Kriete, A., et al., Computer-based cytophotometric classification of thyroid tumors in imprints. Journal of Cancer Research and Clinical Oncology, 1985. 109(3): p. 252-256.

40. Oberholzer, et al., Evaluation of shape descriptors for the morphometric analysis of cell nuclei. Pathology, research and practice, 1986. 181(2): p. 213-22.

CHAPTER 3

Optimizing Debris Filtering in a Quantitative Image Analysis System For Automated Detection of Breast Carcinoma Cells

3.1 INTRODUCTION

Breast conservation therapy (BCT) or removal of part of the breast plus radiation has been established as the standard of care for the surgical treatment of breast cancer [1]. While the overall survival efficacy of BCT has been demonstrated to be equal to full mastectomy (removal of the whole breast) treatment in multiple long term studies, approximately one third of all BCT patients require secondary surgical treatment due to positive margins found with standard pathologic analysis [2-5]. Several methods for the intraoperative analysis of tumor margins have been evaluated to identify the need to resect additional tissue during the initial surgical procedure. Frozen section analysis has been used intraoperatively to successfully lower the re-excision rate [6]; however, frozen section analysis is a difficult and time consuming procedure that is incompatible with traditional post-surgery permanent section analysis as it shaves off the true resected margins during the procedure [7, 8]. Additionally, lengthening surgery times is unfeasible from the standpoint of increasing anesthesia related risk for patients and added hospital expenses. Imprint cytology has also been investigated for intraoperative use with similar accuracy to frozen section analysis [9-

12]. Imprint cytology fully preserves tissue at the margin and, therefore, does not interfere with traditional permanent section analysis. While taking far less time to perform than frozen section analysis, imprint cytology still requires careful manual examination of multiple slides with the accuracy of determining margin status being highly dependent on the experience of the examining cytopathologist [13, 14]. A rapid automated technique to standardize and guide the analysis of a cytopathologist would enable imprint cytology to become a practical intraoperative analysis technique for guiding surgical decisions. However imprint cytology is not a faultless technique. Environmental debris, poor material handling, and staining variation can all introduce imaging artifacts onto a slide that may fluoresce as brightly as properly stained cells when scanned in with a digital system. While a trained human eye can readily distinguish these artifacts from cells, a computer aided diagnosis system requires thorough training to provide high diagnostic accuracy. A previous related study by Cortes-Mateos et. al established that epithelial cell density was a useful metric for determining margin status [15]. In our recent study we established empirical cutoff values for measured properties and used to screen epithelial cells and clusters from other object outlines. An object was rejected as junk if it exceeded the predefined limits for any of these measurements. [16]. The present study focuses on increasing the robustness of the debris filtering process by computing additional statistical measurements for each recognized object, and introducing the use of linear discriminant analysis to optimally distinguish epithelial cell outlines from debris by establishing a numerical parameter constructed from a training set.

3.2 MATERIALS AND METHODS

3.2.1 Surgical Sample Preparation

Institutional Review Board approval from the University of California, San Diego, was obtained to study both breast cancer and non-cancer tissue from patients. All patients underwent their planned procedure for surgical treatment, and specimens were removed and expeditiously sent to the pathology laboratory for analysis. As negative controls, non-cancer samples were acquired from 2 groups: normal tissue was collected from patients undergoing breast reduction surgery and tissue was obtained from patients undergoing prophylactic mastectomy of a noncancerous breast. All surgeries were performed at the University of California San Diego Medical Center. Standard techniques for resection of breast tissue were employed including electric cauterization (Valley Labs, Boulder, Colo., USA). Fresh specimens were gently imprinted onto poly-L-lysine (PLL)-coated glass slides (Newcomer Supply, Middleton, Wisc., USA).

3.2.2 Immunofluorescent Staining

All slides were dual stained with AlexaFluor 488 labeled anticytokeratin antibody (DakoCytomation, Carpinteria, CA) immunofluorescent Cytokeratin and Hoechst 33342 (Invitrogen, Carlsbad, CA) stains. Cytokeratin, an epithelial cell membrane protein, was used to distinguish epithelial cells from leukocytes, adipocytes, fibroblasts and any other cell types that may have been captured during imprint cytology. Hoechst, a nuclear dye, was used to differentiate epithelial cells

from non-cellular debris. The complete staining protocol, as previously reported, took only 20–25 minutes including fixing, permeabilization, and blocking [15].

3.2.3 Touch Preparation for Breast Epithelial Cells

After excision, surgical specimens were grossed in the operating suite by a pathologist. The area with the highest probability of containing tumor cells was located by palpation or by an image-guided wire that was placed preoperatively. A cut through the tumor was made at this location to generate a 'calibrated' positive margin with an area that had a high probability of containing tumor cells. Permanent section pathology was performed on suspicious tissue to verify that cancer cells were present in the calibrated positive margin. Larger tumors were flash frozen for later analysis without further preparation while the suspicious area of smaller tumors was specially inked for later identification. These calibrated margins were made to represent the worst possible outcome: a slice directly through the tumor with no margin of healthy tissue. PLL-coated slides were touched on both halves of the exposed tissue of the cross-sectional cut in a process known as imprint cytology or touch prep. For the permanent section analysis of this same region of tissue, a planar sample of the tissue was sectioned from the tumor surface either for paraffin embedding in a cassette (for T1 tumors, 2 cm or less) or for frozen sectional analysis in a frozen tissue block (for T2 and T3 tumors, greater than 2 cm). In most cases, 4 imprint cytology slides were available for automated analysis. Two slides were taken directly from the tumor surface, and the retained tissue sample was sandwiched between 2 additional slides (**Figure 3.1**). For some small tumors, only 3 imprint cytology slides were taken due to

the small amount of tumor available for study. To ensure that the automated analysis and the standard pathological analysis were compared on the same location in the surgical specimen in all cases, localized pathological analysis was performed by a board-certified pathologist (J.W.R.) to confirm either the presence or absence of cancer from the imprint cytology location. Several 5-micron-thick microtome sections (up to 12) were made through the tissue sample; to insure the most conservative data analysis, if the pathologist found cancer in any of the sections the entire tissue sample was declared positive.

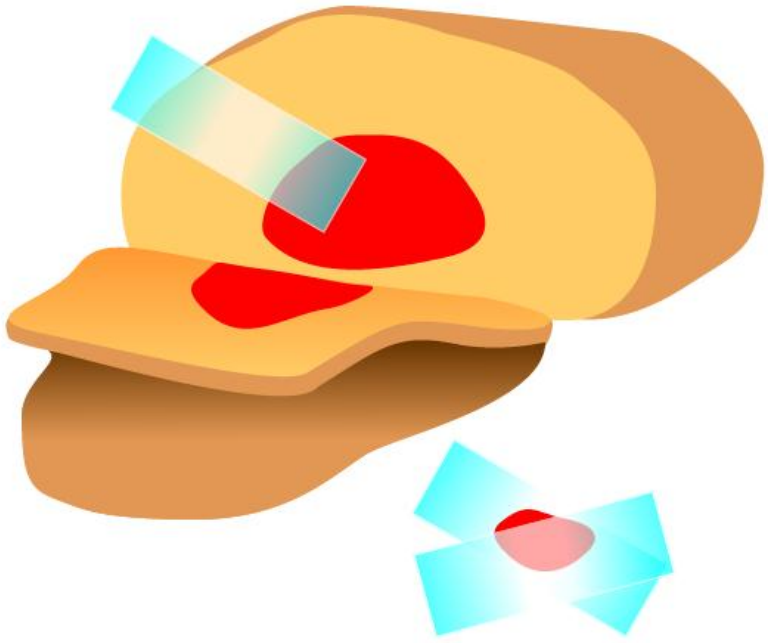

Figure 3.1: Cross sectional slice at suspected tumor location. Touch preps are taken from both sides of the cut, and a small tissue section from the tumor (red) is excised and preserved in a cassette for further analysis (box). One or two touch preps were taken on the excised sample, depending on the size of the tissue removed.

3.2.4 Automated Microcopy and Image Acquisition

An automated scanning stage microscope was used to digitize each imprint cytology slide (AxioImager Z1, Carl Zeiss Inc., Thornwood, NY). The entire surface of each touch prep slide was imaged at a magnification of 5x using a 1.4 megapixel camera (Cool-SNAP HQ2, Photometrics, Pleasanton, CA) for an imaging resolution of 1.267μm / pixel. Automated control of the microscope was handled by a custom software application. Prior to acquisition, a few focus points for the slide were determined manually along with appropriate exposure times for each fluorescent channel to maximize sensitivity to staining intensity and to establish the scanning limits for each slide. The slide surface was automatically partitioned into a grid of image tiles covering the selected area, and two fluorescent images (one for Hoechst fluorescence and one for Cytokeratin fluorescence) were recorded at each image tile. Once acquisition was started, the control program employed a software autofocusing based on well-known techniques to obtain reliable focus at each image tile [17, 18]. As depicted in **Figure 3.2**, the software autofocusing implementation consists of acquiring a z-stack and processing each image with a convolution filter using a 3x3 square kernel. The z-heights from the manually established focus points were interpolated across the slide surface and used as a rough initial estimate of the focal plane to center the z-stack of a given image tile around. The summation of the squared intensity values in the convoluted image were taken as the relative sharpness index of the image, and the image with the highest sharpness index was chosen as the sharpest image. This is a simple and established method which has the advantage of ease of

implementation and speed. Although the sharpness index method was not specifically assessed for accuracy compared to more advanced methods or manual focus, the results of this study show it is accurate enough at low imaging resolution for the automatic classification technique to be effective.

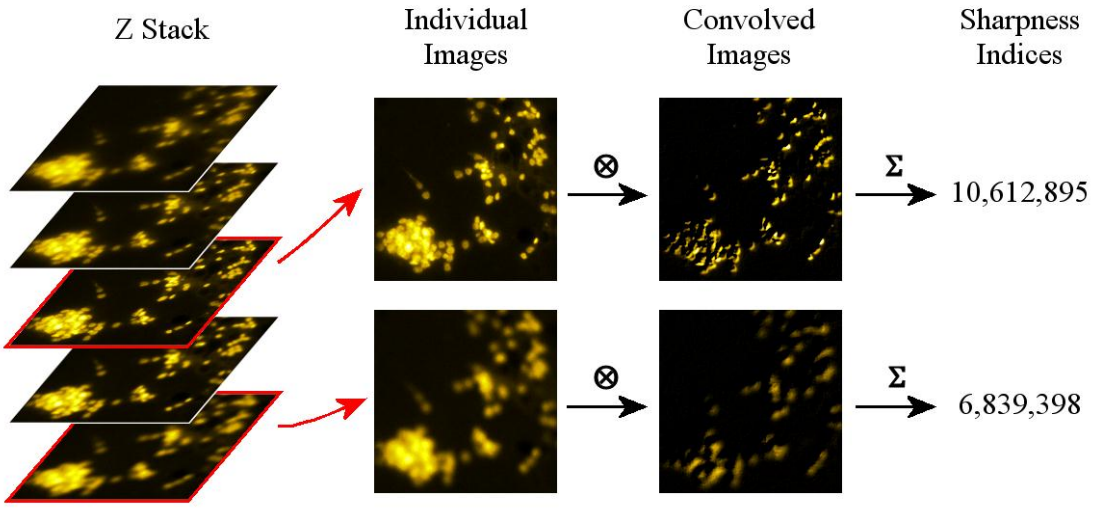

Figure 3.2: Determining the optimal focal plane. Software autofocusing was employed in our custom microscope control application to obtain reliably focused images. As depicted, a z-stack was acquired, and each image was processed with a convolution filter using a 3x3 square kernel to reveal the high frequency content (i.e. object edges) of the image. The sum of the squares of the pixel values in the convoluted image was used as a measure of the relative sharpness of the image. The image with the highest sharpness index was selected.

3.2.5 Automated Image Processing and Segmentation

Raw fluorescent images were found to contain a mixture of specifically stained epithelial cells, non-specific stained cells, non-cellular debris, and empty space. By employing standard image processing operations and segmentation (enumerated below), grouped areas of pixels could be identified for each object in an image, and were subsequently measured for classification as cellular or non-cellular. Image

processing and segmentation was performed on fluorescence images from the Cytokeratin channel as follows: (**Figure 3.3**)

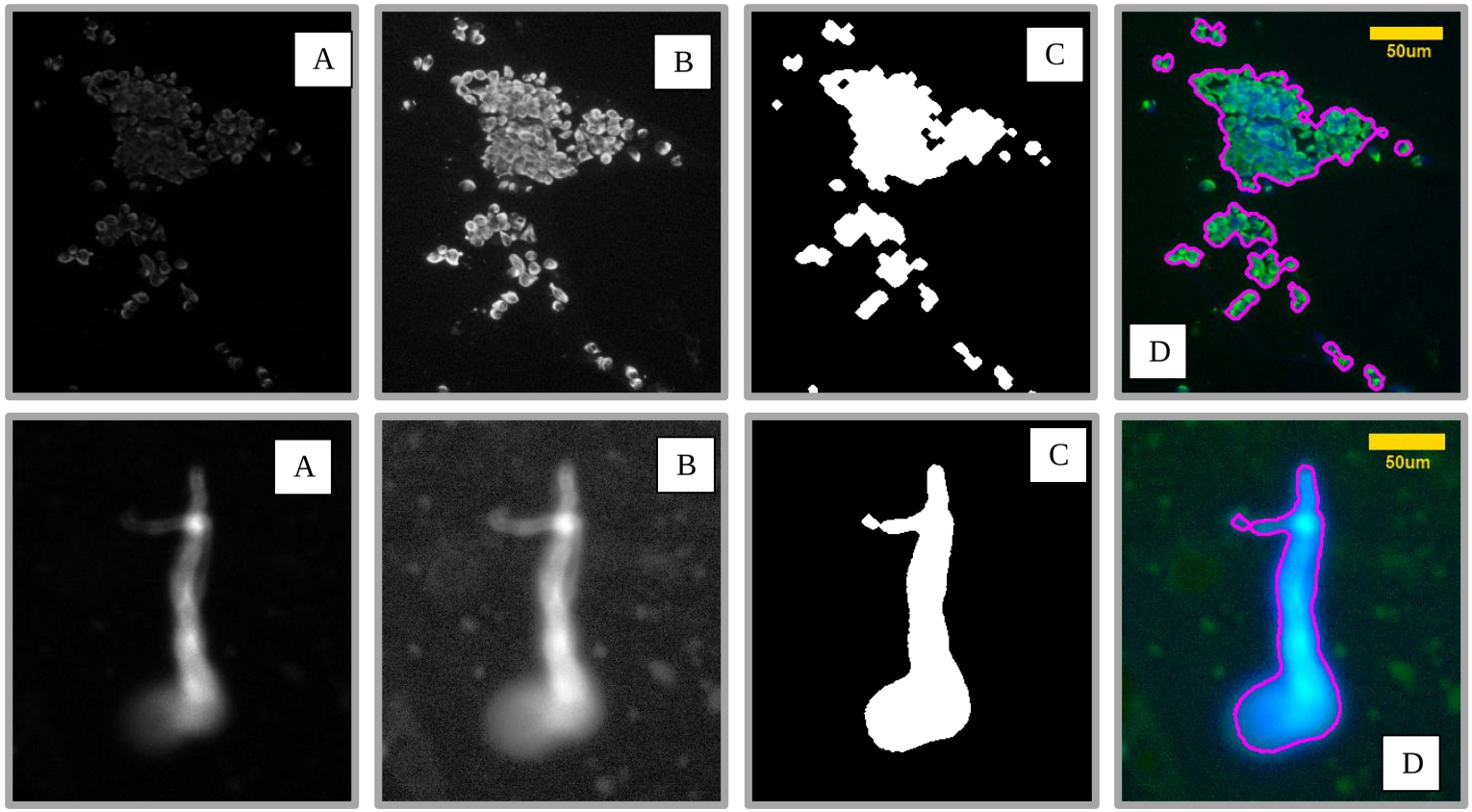

Figure 3.3: Object Outlining from Cytokeratin Images.
(Top) Epithelial cell clusters. (Bottom) Out of focus fiber.
A) original B) contrast enhanced image after histogram equalization C) Binary image after morphological operations D) Recognized object outlines mapped back to combined fluorescence image. Software cannot distinguish between cells and debris at outlining stage.

(1) A background estimation of the raw fluorescence image was performed by measuring fluorescence intensity across an evenly spaced sampling grid consisting of 10% of the pixels in the image. The background was determined to be the average of the lowest 10% intensity pixels in the sampling grid. The background value was stored for later use.

(2) Although all images were saved in 14-bit grayscale format (0-16383 value range), the effective value range of images varied drastically due to illumination, exposure time, and focal differences both within individual slides and between different slides. Histogram equalization, a well established technique for image contrast enhancement, was employed to normalize intensity values across the full value range [19]. By redistributing higher occurring intensity values across several values while concentrating less frequently occurring values into groups, histogram equalization can dramatically enhance global image contrast [20]. The adjusted background value of the histogram equalized image was also computed and stored so that corrected intensity ratios could be compared between objects.

(3) Renyi entropy was used to determine a suitable threshold value for use in binary conversion of each image [21]. Renyi entropy selected for its effectiveness in calculating a suitable threshold value for most images, including images consisting of sparse single cells as well as images with high density clusters of cells.

(4) A 3x3 square median filter was applied to the binary image to remove any single pixel grain noise resulting from the thresholding operation [22]. Two binary morphological operators were applied to the image in order to connect disjoint sets of pixels: a binary closure followed by a binary opening [19]. Both operations were performed with a 3x3 cross structuring element. A connected component algorithm, wherein an image is segmented by adjacent white pixels grouped together to create sets of object pixels, was applied to obtain outlines of objects in the binary image [23].

(5) For each recognized object in the image, several measurements were computed and stored for statistical analysis. The pixel coordinates contained in each object outline were mapped back to the histogram equalized fluorescent cytokeratin and Hoechst images and the mean cytokeratin fluorescence (cyto_mean) and mean Hoechst fluorescence (hoechst_mean) were recorded. These values were divided by the estimated background value of the histogram equalized images to calculate how many multiples above background an object's intensity was (cyto_bg_r and hoechst_bg_r). The correlation coefficient between the cytokeratin and Hoechst intensity values (cyto_hoechst_corr) was computed from each objects raw fluorescence images. This was an important metric for identifying multispectral debris such as air bubbles, dust, and fibers. Any object with a mean intensity less than twice the background estimate for either cytokeratin or Hoechst intensity was rejected as background noise. Additionally, any object with a mean raw intensity value greater than 10,000 for either cytokeratin or Hoechst was rejected for being overexposed. These values were optimized for the Zeiss AxioImager Z1 and Cool-SNAP HQ2

Photometrics camera combination used to scan in all patient slides by inspecting exposure conditions, saturation, and dynamic range across a variety of images, and would need to be re-optimized for a different microscopy platform. Lastly the circularity of the object was stored to provide geometric information during object classification.

3.2.6 Statistical Delineation between Cellular and Non-Cellular Areas

Epithelial cells tended to pull off in large clusters during imprint cytology for most positive cancer cases as opposed to single isolated cells. Additionally, imprint cytology can be an inherently messy process with cytological debris (fragments of fat, necrosis, fibrin, fragmented cytoplasmic material, non-specific staining) along with non-cytological debris (fibers, air bubbles, unwashed dye pooling) imparting on the slide surface along with any epithelial cells. Due to these factors, the image processing and segmentation of the automated analysis technique was optimized simply to outline all illuminated objects in any given image, and measured statistical properties were employed to classify each object as either cellular or non-cellular in a process referred to hereafter as debris filtering. In a previous study, manual cutoff values for circularity, cytokeratin coefficient of variance, Hoechst coefficient of variance, and Cytokeratin-Hoechst correlation were established and used to screen epithelial cells and clusters from other object outlines [16]. An object was rejected as junk if it exceeded the predefined limits for any of these measurements. The present study focuses on increasing the robustness of the debris filtering process by constructing a

training of manually classified cellular and non-cellular objects. Measurements from these two classes in the training set were used to optimize a linear discriminant analysis (LDA) parameter [24]. Measurements for each object in the final patient dataset were remapped to discriminant parameter space, where they were compared to discriminant parameter values from the training set for classification as either cellular or debris.

3.3 RESULTS AND DISCUSSION

3.3.1 Classification of Debris vs. Cells

An extra sample slide each from representative IDC, DCIS, LCIS, and normal patients (4 slides total) was analyzed with the image recognition software up to the object recognition step. Outlines of each object were then drawn back on their respective images and visually inspected to see if they contained individual epithelial cells, epithelial cell clusters, or various types of debris. Objects that clearly contained cells and no debris were classified as "cellular" while objects that clearly contained debris or other imaging artifacts, with or without cells, were classified as "non-cellular". Indeterminate objects were ignored. A training set of 1398 cellular objects (64.8% prior probability) and 759 non-cellular objects (35.2% prior probability) was obtained from this classification and used to construct a linear discriminant analysis (LDA) function. A linear discriminant function was derived from the composite cellular and non-cellular training set. Six measurements of each classified object were used to construct the linear function: circularity, cytokeratin coefficient of variation

(cyto_cv), Hoechst coefficient of variation (hoechst_cv), cytokeratin intensity to background ratio (cyto_bg_r), Hoechst intensity to background ratio (hoechst_bg_r), and raw cytokeratin to Hoechst intensity coefficient of correlation (cyto_hoechst_corr). The cyto_cv, hoechst_cv, cyto_bg_r, and hoechst_bg_r parameters were measured from histogram equalized images while cyto_hoechst_corr was taken from original fluorescence images (**Table 3.1**).

Table 3.1: Linear Discriminant Analysis results. The overall linear discriminant score for an object is computed by subtracting the weighted means of each measurement (circularity, etc) from the observed values for a given object, multiplying these differences by the linear discriminant coefficient (LD1) for each variable, and summing the resulting terms. The LD score can then be used to classify the object as either cellular or debris.

Variable	LD1	Cellular Means	Non-Cellular means
circularity	-2.33	0.662	0.519
cyto_cv	-2.19	0.177	0.148
hoechst_cv	-6.49	0.343	0.178
cyto_bg_r	0.00338	17.6	13.4
hoechst_bg_r	0.0132	11.1	15.8
cyto_hoechst_corr	2.18	-0.0751	0.623

Examination of the correlation coefficients of the variables in the test set revealed differences between the fluorescent properties of cells and debris (**Table 3.2**). Circularity was anti-correlated with cytokeratin_cv for cells, as large variations in fluorescent staining was seen across cells and their membranes in large clusters which tended to be less circular as compared to single cells which were generally highly

circular with a ring of fluorescence around the nucleus. This effect is not seen across the many kinds of debris. Cyto_cv and hoechst_cv are correlated, as are circularity and cyto_hoechst_corr in the debris class. These are characteristic features of dust and fibers, which strongly reflect both cytokeratin and Hoechst fluorescence. Fiber and dust debris looked highly similar in both channels to the naked eye. LDA works by redistributing linear combinations of measurement variables to maximize the separation between classes. Intrinsic differences between classes increases the likelihood of obtaining a high performing discriminant function.

Table 3.2: Correlation Matrices for Cellular and Non-Cellular Objects. Variables used in LDA classification exhibit different trends in debris objects and cellular objects. For example, cellular objects were seen to have circularity anti-correlated with cytokeratin coeff. of variation while. Single epithelial cells (highly circular) are characteristically imaged as a single ring of fluorescence while cell clusters have irregular object outlines and a higher degree of fluorescence variation. No relation between cytokeratin fluorescence and circularity is observed for debris.

Debris / Cells	circularity	Cytokeratin Coeff. Variation	Hoechst Coeff. Variation	Cytokeratin to Background Ratio	Hoechst to Background Ratio	Cytokeratin to Hoechst Correlation
circularity	1.00 / 1.00	-0.06 / -0.58	-0.21 / -0.01	-0.11 / -0.03	-0.48 / -0.01	0.41 / 0.04
Cytokeratin Coeff. Variation	-0.06 / -0.58	1.00 / 1.00	0.55 / 0.20	0.41 / 0.27	-0.06 / -0.02	0.31 / -0.02
Hoechst Coeff. Variation	-0.21 / -0.01	0.55 / 0.20	1.00 / 1.00	0.16 / 0.15	0.12 / -0.02	0.02 / 0.14
Cytokeratin to Background Ratio	-0.11 / -0.03	0.41 / 0.27	0.16 / 0.15	1.00 / 1.00	0.12 / 0.07	-0.07 / -0.20
Hoechst to Background Ratio	-0.48 / -0.01	-0.06 / -0.02	0.12 / -0.02	0.12 / 0.07	1.00 / 1.00	-0.24 / 0.14
Cytokeratin to Hoechst Correlation	0.41 / 0.04	0.31 / -0.02	0.02 / 0.14	-0.07 / -0.20	-0.24 / 0.14	1.00 / 1.00

The resulting discriminant function obtained from the training set had a class prediction accuracy of 94.5% with leave-one-out prediction and a singular value of 67.3 (between class variance to within class variance ratio). These values indicate a strong fit of the discriminant function to the training set. Cellular objects exhibited a broader distribution of LDA values with a coefficient of variance of 97% compared to 46% for non-cellular objects. This is likely due to grouping cell clusters of all sizes together with single cells in the cell training class, despite differences in their fluorescent properties. Regardless, the cellular training object mean was -1.07 and non-cellular object mean was 1.97; a two sided t-test for unequal variances showed a highly significant difference between the two populations with $p < 0.0001$ (**Figure 3.4**). A cutoff value of -0.024 (1 standard deviation away from the cellular mean) was chosen to slightly bias the software towards over classifying objects as debris. Any object with a linear discriminant parameter less than this cutoff value was accepted as an epithelial cell when counting cells on a slide.

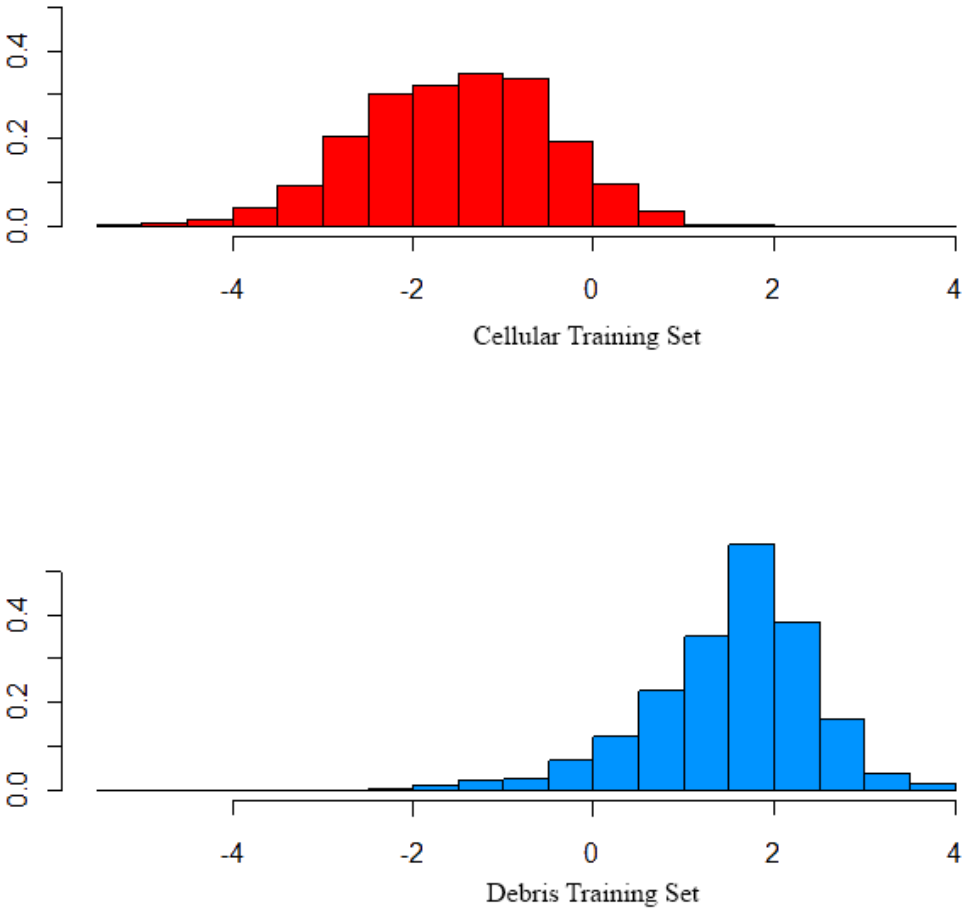

Figure 3.4: LD1 distributions of training set. The cellular group of the training set consisted of individual epithelial cells as well as clusters ranging in size from a few cells to hundreds of cells. The cellular training group exhibited a wider distribution than the non-cellular group. However a 2 sided t-test showed a highly significant difference between the two groups with $p < 0.0001$.

The LDA value for each object in the overall patient dataset was calculated, and used to classify each object as either cellular or non-cellular when calculating cell counts. After classification, raw density (total area of all objects divided by slide

surface area) and cellular density (total area of cellular objects divided by slide surface area) were calculated for each slide. As seen in **Figure 3.5**, the raw density and cellular density for positive cancer cases was highly similar: positive cancer slides contained mostly cellular objects. The overall filter ratio (cellular density to raw density) for positive cancer cases was 0.64 while the filter ratio for non-cancer and negative cancer cases was only 0.18. Crucially, several prophylactic and normal cases were initially seen to have a high raw object density. When manually examining the images from these cases, the raw density was seen to consist largely of debris with very few actual cells present. Under the microscope, the slides for these cases appeared largely empty. With no cells present for autofocusing; therefore, the automated microscopy software tended to focus on debris located on the slide coverslip or large air bubbles introduced during drying steps rather than choosing a focal plane with no spectral content. Filtering with the LD cutoff value removed the vast majority of debris from negative cases, while preserving the vast majority of cells in positive cancer cases.

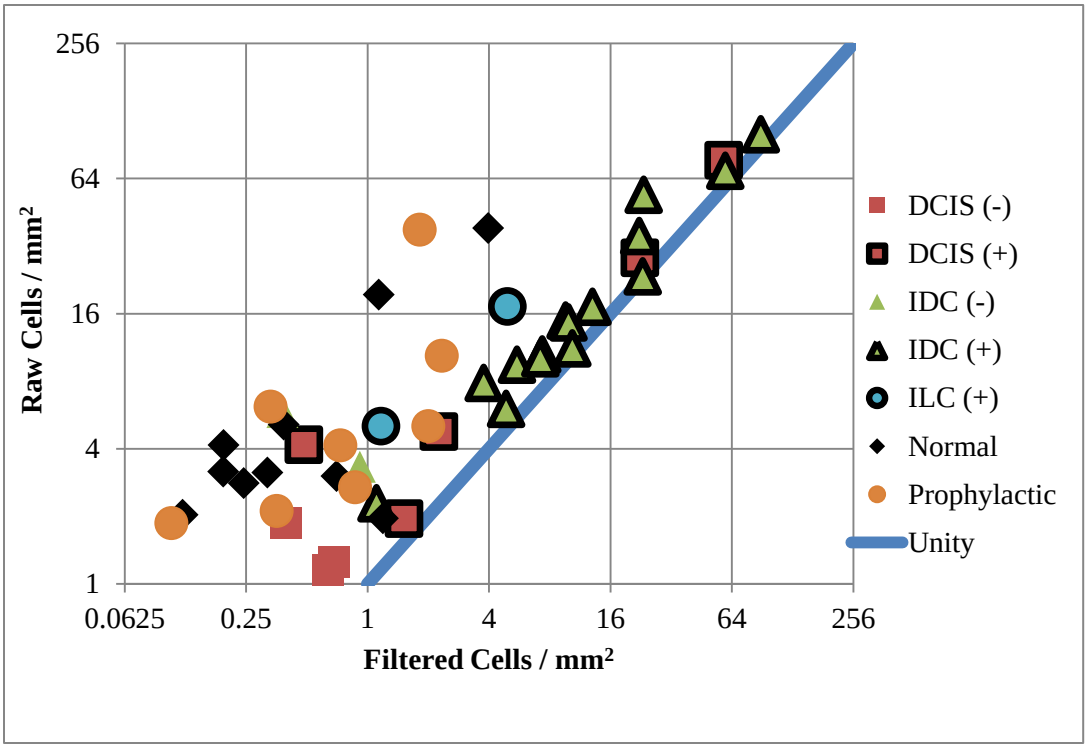

Figure 3.5: Cellular densities before and after debris filtering. Cellular density was compared before (Raw Epithelial Cells / mm^2) and after (Filtered Epithelial Cells / mm^2) automated debris filtering. For most cancer cases, debris filtering had a relatively small impact on cellularity while up to a 25x decrease was observed for non-cancer cases. Several normal and prophylactic cases were found to have large amounts of dust, fibers, and non-specific staining which resulted in high cellularity measurements before filtering. Automated filtering of image outlines eliminates false positives from non-cellular debris on touch prep slides.

3.3.2 Epithelial Cell Density

In order to evaluate the overall efficacy of the classification technique for evaluating patients, results were compared to final diagnosis by a skilled pathologist. Each cancer case was determined to be either positive if cancer was present in any degree in permanent section analysis, and declared negative otherwise. All prophylactic and

breast reduction cases were used as negative controls. On average, the positive cancer cases were found to have 17.35 epithelial cells / mm2 while the negative cases only had 0.369 cells / mm2 with standard deviations of 22.94 (132%) and 0.156 (42.3%) respectively. A two sided t-test for unequal variances showed a significant difference between the two populations with $p = 0.0031$. Comparatively, a t-test with the manual filer cutoff values applied to the same raw object set only exhibited a p value of 0.0129. From the standpoint of differentiating between positive and negative patients, the linear discriminant method exhibited higher separating performance than the manual cutoff method when considering filtered cell density alone.

3.3.3 Suspicious Object Coverage

While a very significant difference between positive and negative cases was found using only average filtered cell density, a secondary metric was calculated to increase robustness in identifying cancer cases. By choosing a more aggressive cutoff value for the linear discriminant parameter, the LD scores of each recognized objected can be utilized in a separate manner from simply discarding debris outlines. For the established discriminant function, the lesser a LD value a given object has, the more it resembles cellular objects classified in the training set. Additionally, visual inspection of slides revealed that positive cancer cases tended to have epithelial cells distributed across a large fraction of imprint slide surfaces, while negative cases tended to have only a few small clusters of epithelial cells. To capture this information, a suspicious cell coverage parameter was calculated for each case by using LD cutoff value of -1.07 (the average LD score of cellular objects in the training set), and counting the

percent of image tiles for a given slide having at least 1 cell with a LD score < -1.07. The positive group mean was 36.9% with a standard deviation of 15.6% while the negative group mean was 4.3% with a standard deviation of 4.05%. A two tailed p value less than 0.0001 again demonstrated an extremely significant difference between the positive and negative patient groups using this parameter.

Filtered epithelial cell density and suspicious object coverage were calculated for a total of 29 positive cancer cases, and 18 non-cancer cases. By plotting epithelial cell density versus the suspicious object coverage score for each case, the separation between the positive and negative populations can be visualized, and a discriminant line can be clearly drawn using Fischer's method (**Figure 3.6**). All data points above the discriminant line were judged to be positive while all data points below the cutoff line were judged to be negative. This robust method for detecting positive cases proved to be highly accurate, with accuracy for invasive cancers being 95%. This detection method produced no false positives; however 3 false negatives were observed (**Table 3.3**). Additional cuts on permanent section analysis of the single false negative invasive ductal carcinoma (IDC) case revealed only a small population of cancerous cells in approximately 1% of the observed tissue. Permanent section analysis of the two false negative ductal carcinoma in situ cases found only single focuses of low grade DCIS in each case. All false negative cases exhibited a low cellular density not only calculated from the automated technique, but also when inspected manually. While this presents a limitation in using epithelial cell density as a detection parameter, the overall accuracy results are still very high. From the standpoint of using this technique intraoperatively, any cases reported as negative

through automated analysis could quickly be reviewed by a pathologist by presenting a list of the most suspicious objects found on a slide. Additionally, any cancer cases missed as false negatives would still be found through traditional pathology analysis.

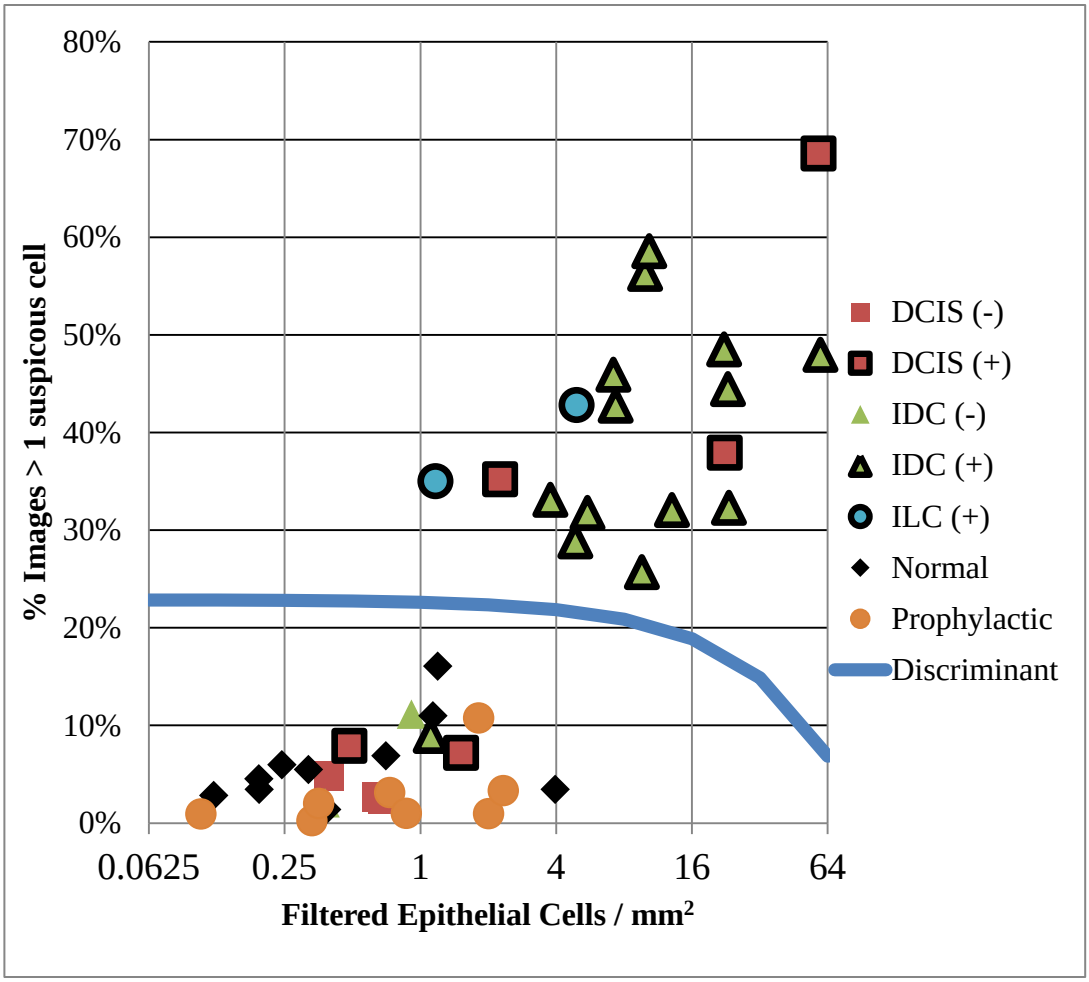

Figure 3.6: Two-dimensional discrimination for cancer detection: % Images/tiles (xx um2) > 1 suspicious cell vs. filtered cells / mm^2 averaged across the whole slide. Using two measurements produces a clear separation between positive cancer cases (data points with black outlines) and non-cancer and negative cancer cases (normal, prophylactic, and non-outlined data points). No false positives and only 3 false negatives were observed. False negatives are black outlined symbols below the cutoff line.

3.4 CONCLUSION

The presented automated analysis technique produced highly accurate results for detecting fluorescently stained epithelial cells on imprint cytology slide surfaces. The combination of a fast image processing algorithm with an optimized classification method for separating debris from true cellular measurements provides a robust method for a technique to aide clinical decision making while preserving patient specimens for traditional pathology analysis. This technique was presented as a way to translate into clinical settings for real time intraoperative cell analysis. Furthermore, the training method described in this paper could readily be employed to other kinds of fluorescently stained samples containing a heterogeneous mixture of objects or cells that can be found in clinical patient samples.

3.5 ACKNOWLEDGEMENTS

Chapter 3, in full is currently being prepared for submission for publication of the material. Martin, David T.; Ta, Casey N.; Sandoval, Sergio; Ruidiaz, Manuel E.; Messmer, Davorka; Kummel, Andrew C.; Blair, Sarah L.; Wang-Rodriguez, Jessica. The dissertation author was the primary researcher and author of this material.

3.6 REFERENCES

1. Lichter, A.S., et al., Mastectomy versus breast-conserving therapy in the treatment of stage I and II carcinoma of the breast: a randomized trial at the National Cancer Institute. J Clin Oncol, 1992. 10(6): p. 976-983.

2. Fisher, B., et al., Twenty-Year Follow-up of a Randomized Trial Comparing Total Mastectomy, Lumpectomy, and Lumpectomy plus Irradiation for the Treatment of Invasive Breast Cancer. N Engl J Med, 2002. 347(16): p. 1233-1241.

3. Carl, M.M., et al., Ten-year results in 1070 patients with stages I and II breast cancer treated by conservative surgery and radiation therapy. Cancer, 1995. 75(9): p. 2328-2336.

4. Smitt, M.C. and K. Horst, Association of Clinical and Pathologic Variables with Lumpectomy Surgical Margin Status after Preoperative Diagnosis or Excisional Biopsy of Invasive Breast Cancer. Ann Surg Oncol, 2007. 14(3): p. 1040-1044.

5. Funda, M., et al., Positive surgical margins and ipsilateral breast tumor recurrence predict disease-specific survival after breast-conserving therapy. Cancer, 2003. 97(4): p. 926-933.

6. Olson, T., et al., Frozen Section Analysis for Intraoperative Margin Assessment During Breast-Conserving Surgery Results in Low Rates of Re-excision and Local Recurrence. Annals of Surgical Oncology, 2007. 14(10): p. 2953-2960.

7. Thornburg, W. And P.E. Mengers, An Analysis Of Frozen Section Techniques: I. Sectioning Of Fresh-Frozen Tissue. Journal Of Histochemistry & Cytochemistry, 1957. 5(1): P. 47-52.

8. Weber, S., Storm, F K, Stitt, J, et al, The role of frozen section analysis of margins during breast conservation surgery. The cancer journal from Scientific American, 1997. 3(5): p. 2730277.

9. D'Halluin, F., et al., Intra-operative touch preparation cytology following lumpectomy for breast cancer: A series of 400 procedures. The Breast, 2009. 18(4): p. 248-253.

10. Cox, C., et al., Cytologic evaluation of lumpectomy margins in patients with ductal carcinoma in situ: Clinical outcome. Annals of Surgical Oncology, 1997. 4(8): p. 644-649.

11. Muttalib, M., et al., Intra-operative assessment of excision margins using breast imprint and scrape cytology. The Breast, 2005. 14(1): p. 42-50.

12. Weinberg, E., et al., Local recurrence in lumpectomy patients after imprint cytology margin evaluation. The American Journal of Surgery, 2004. 188(4): p. 349-354.

13. Klimberg, V., S. Harms, and S. Korourian, Assessing margin status. Surgical Oncology, 1999. 8(2): p. 77-84.

14. Klimberg, V.S., K.C. Westbrook, and S. Korourian, Use of touch preps for diagnosis and evaluation of surgical margins in breast cancer. Annals of Surgical Oncology, 1998. 5(3): p. 220-226.

15. Cortes-Mateos, M., et al., Automated Microscopy to Evaluate Surgical Specimens Via Touch Prep in Breast Cancer. Annals of Surgical Oncology, 2009. 16(3): p. 709-720.

16. Martin, D.T., et al., Quantitative Automated Image Analysis System with Automated Debris Filtering for the Detection of Breast Carcinoma Cells. Acta Cytologica, 2011. 55(3): p. 271-280.

17. Price, Comparison of phase-contrast and fluorescence digital autofocus for scanning microscopy. Cytometry, 1994. 16(4): p. 283-283.

18. Shen, F., L. Hodgson, and K. Hahn, Digital Autofocus Methods for Automated Microscopy, I. James, Editor. 2006, Academic Press. p. 620-632.

19. R. C. Gonzalez, P.W., Digital Image Processing. 2nd ed. 1987, Reading, Massachusetts: Addison-Wesley Publishin Co.

20. Zimmerman, J.B., et al., An evaluation of the effectiveness of adaptive histogram equalization for contrast enhancement. Medical Imaging, IEEE Transactions on, 1988. 7(4): p. 304-312.

21. Sahoo, P., C. Wilkins, and J. Yeager, Threshold selection using Renyi's entropy. Pattern Recognition, 1997. 30(1): p. 71-84.

22. Gary A, M., Adaptive filters for digital image noise smoothing: An evaluation. Computer Vision, Graphics, and Image Processing, 1985. 31(1): p. 103-121.

23. Dillencourt, M.B., H. Samet, and M. Tamminen, A general approach to connected-component labeling for arbitrary image representations. J. ACM, 1992. 39(2): p. 253-280.

24. Lachenbruch, P.A. and M. Goldstein, Discriminant Analysis. Biometrics, 1979. 35(1): p. 69-85.

CHAPTER 4

Fabrication of Silicon on Borosilicate Glass Microarrays for Quantitative Live Cell Imaging

4.1 ABSTRACT

Planar arrays of microwells were fabricated in Silicon on borosilicate glass (pyrex) substrates in order to facilitate live cell fluorescence imaging experiments for cells sequestered inside their own individual microenvironments for incubation and quantification of single cell secretions. Two methods of deep silicon etching were compared: cryogenic deep reactive ion etching (DRIE) and time multiplexed DIRE (Bosch Process). A 200um Si wafer was bonded to a 500um pyrex substrate. Cryogenic DRIE allowed for the reliable fabrication of 75-100um deep microwells with 60x60um openings across a 10x10mm substrate while the Bosh Process allowed for etching entirely through the Si layer, producing 200um deep microwells with transparent bottoms and steep sidewalls while maintaining the target 60x60um opening geometry.

4.2 INTRODUCTION

Investigating cancer from a systems biology perspective has been hindered by the lack of tools for a dynamic multiplexed analysis of surface and secreted proteins from small numbers of tumor cells. Several existing techniques such as flow

cytometry, ELISA, or ELISPOT have been well established to measure to quantify secretants from a population of cells or detect surface protein expression. However, none of these techniques are suitable for quantifying secretants from individual cells or performing repeated measurements on live cells [1-5]. With this aim in mind, a planar microarray platform was designed to sequester cells in their own microenvironment to perform live cell imaging experiments to quantify secretant levels and detect surface protein expression in response to stimuli (**Figure 4.1**).

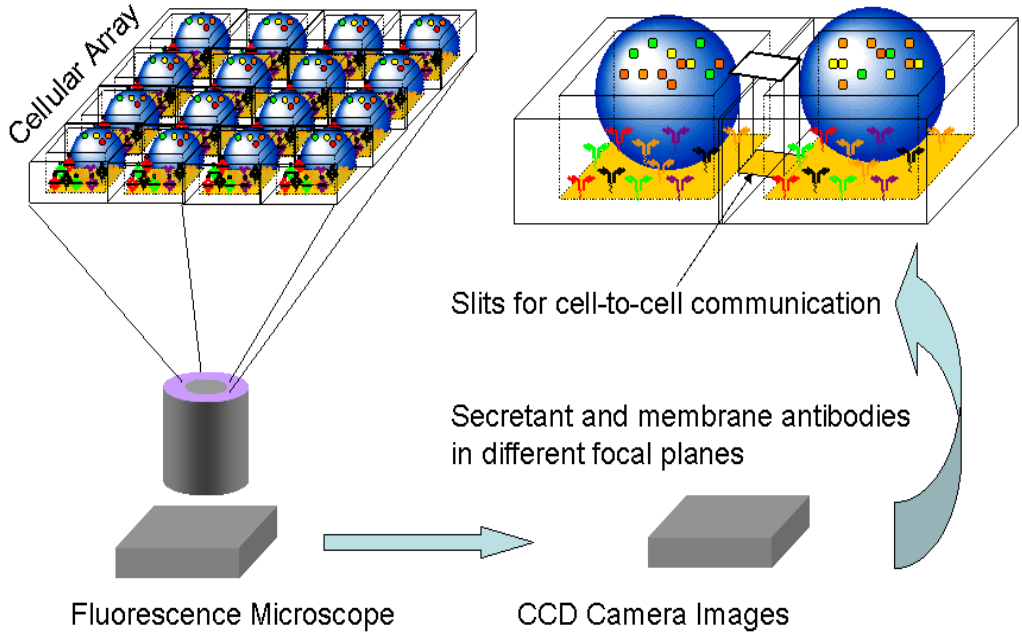

Figure 4.1: A planar array of microwells can contain individual cells in their own microenvironment for automated fluorescence based quantification of secretants. Cell-cell communication experiments can be conducted by opening diffusion slits between adjacent microwells.

An array of 60x60um square openings separated by 20um across a 10x10mm substrate consists of 15,625 different microwells on a single chip. The grid separation allows for easy image segmentation of each microwell with standard image processing

techniques, and allows for quantitative measurements across multiple fluorescent channels. While plating cells in solution would lead to a random distribution across the microarray, the number of cells in each microwell can be easily counted through surface membrane staining; any microwell that did not contain only a single cell can be automatically filtered out from analysis. On chip cell staining and multiday survival have been demonstrated on microarrays 100um deep and a well opening to depth ratio of 10:1.

4.3 EXPERIMENTAL DETAILS

A 200um thick Si wafer was bonded to a 500um thick pyrex wafer, and subsequently diced into 12.5x12.5mm chips for individual sample preparation. A chromium hard mask was selected for cryogenic etching and microwell patterns consisting of 50x50um square openings separated by a 10um grid, and 60x60um square openings separated by a 20um grid were transferred to the chromium hard mask pattern through standard photolithographic techniques. The samples were mounted to a carrier wafer with vacuum oil and cryogenically etched with an Oxford P100 ICP Tool (Oxfordshire, UK). Etching parameters were established through the black silicon method [6], with a 1250W ICP power, 10W forward biasing power, 50 sccm SF6 flow rate, 6 sccm O2 flow rate, chamber pressure of 12mTorr, and cryogenic carrier wafer cooling at -115° C. Total etching time was varied from 45 to 120 minutes to achieve differing final depths.

Samples for Bosch process etching were prepared with a SiO_2 hard mask. The silicon surfaces of the samples were coated with a 1.5 um thick plasma enhanced chemical vapor deposition (PECVD) SiO_2 layer. The SiO_2 was patterned by optical lithography by 60x60um squares separated by a 20um grid. The SiO_2 was etched using an inductively coupled plasma (ICP) dry etching tool with a CHF_3-based etch recipe with a Panasonic ICP Tool (Osaka, Japan). After photoresist removal, the samples were etched with a Plasmatherm SLR Series DRIE (St. Petersburg, Florida) with a Bosch process recipe. An initial passivation polymer deposition step was employed in which 70 sccm of C_4F_8, 0.5 sccm SF_6, and 40 sccm Ar were flowed into the chamber under 825W of ICP power for 5 seconds. The C_4F_8 flow rate was reduced to 0.5 sccm, and the SF_6 flow rate was cycled between 50 sccm for 2 seconds (polymer re-deposition step), to 100 sccm for 6 seconds (etching step) for a total time of 2 hours. ICP power was held at 825W, forward bias was held at 9W, and the sample chuck was held at 20°C. Process parameters were first optimized on plain silicon substrates to minimize material costs.

After etching with the cryogenic or Bosch processes, samples were examined under optical microscopy and subsequently cleaved for sidewall examination with an electron microscope.

To test cell surface marker staining and multiday survival, 100um deep microwells fabricated in silicon using the Bosch process. THP-1 cells were incubated with Alexa488 conjugated MHC-class I antibody for 30 minutes as a positive staining control or with a non-specific Ig antibody as a negative control on separate microwell arrays. Both arrays were imaged under a fluorescent microscope without washing of

any unbound antibody to test the ability to stain without removal of any cellular secretants. Cells were also plated onto a microarray and incubated for 5 days at 37°C inside a CO_2 incubator in culture media. A 50uL drop of propidium iodine (PI), a viability stain, was dispersed onto the microarray and imaged 5 minutes later under a fluorescent microscope. This viability test was repeated with the addition of dead cells at the end of 5 days to verify proper PI staining.

4.4 DISCUSSION

Smooth, straight, and intact sidewalls that closely corresponded to the target microwell dimensions were critical to determine the total incubation volume of the microwells. Additionally, because accurate quantification of secretants was the ultimate goal, the microwell platform needs to be compatible with the highest resolution inverted confocal fluorescence microscope systems. Confocal microscopy not only has advantages in spatial resolution over conventional microscopy, but is also less susceptible to picking up out of focus background signal while allowing for increased scanning speed in automated systems [7]. For these reasons, a microwell architecture of silicon/pyrex substrates was proposed to allow for optimal imaging quality through transparent bottoms of the microwells. Through microfluidic dynamic simulations, it was determined that a microwell depth to opening length ratio of 10:1 was required to keep a majority of cellular secretants at the bottom of microwells for at least a minute before diffusion could significantly lower secretant concentration at

the bottom of microwells. The secretant diffusion was modeled with the following equation:

$$c_t = \nabla^2 c = \frac{1}{r}\frac{\partial}{\partial r}\left(r\frac{\partial c}{\partial r}\right) + \frac{\partial^2 c}{\partial z^2} \quad (1)$$

where ct = concentration at time t, r = dimensionless radius, z = microwell height (z=0 at the top of the well). Solving numerically for a microwell with 10:1 height to opening ratio at 55 seconds shows 90% of a 15kD secreted protein remains at the bottom of a well. At 448 seconds only 10 of the secreted protein remains at the microwell bottom. In general, the diffusion time scales as (height/opening) ^{2}.

4.4.1 Cryogenically Etched Samples vs Bosch Process Samples

The cryogenic etching process was found to be reliable in fabricating microwells with a depth from 75-100um with an average etching rate of 1.4um/min with both 50x50um and 60x60um square openings and a microwell depth to opening length to ratio between 1:1 and 2:1. However, the cryogenic process proved to be inconsistent when etching microwells with high aspect ratios (depth to opening length). Under identical process parameters (gas flow rates, plasma powers, and cooling temperature), a variety of defects were observed for etches lasting longer than 90 minutes (**Figure 4.2**).

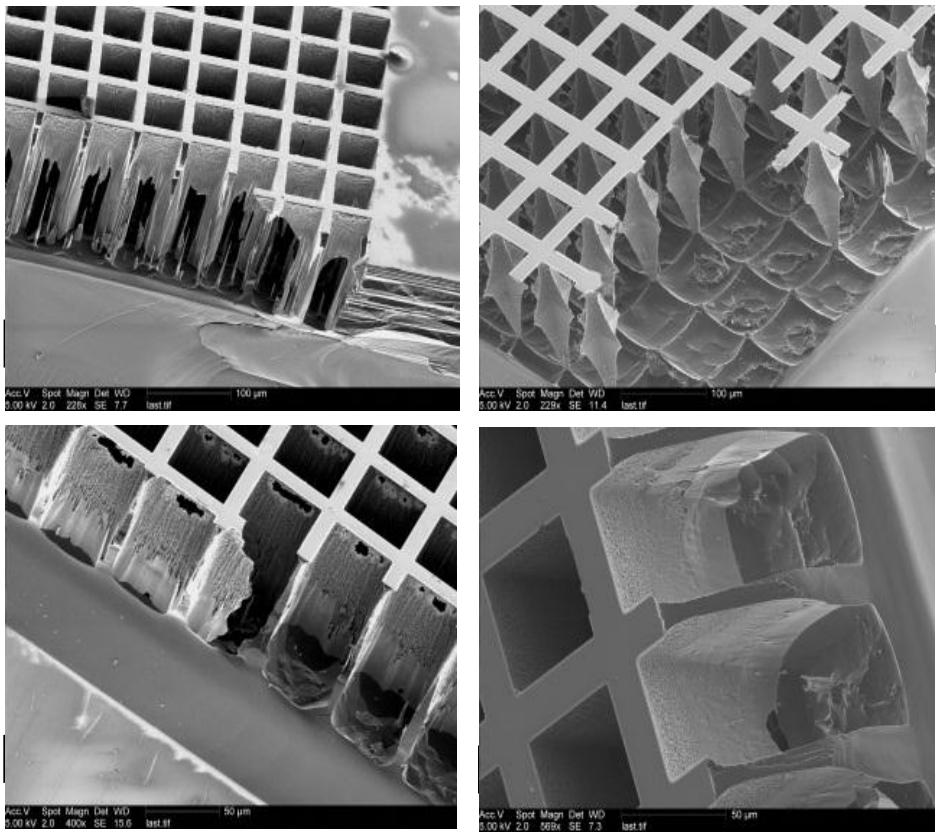

Figure 4.2: Cryogenically etched samples etched under identical process parameters. (A) Bottom sidewall punch through. (B) Pillaring and total wall punch through. (C) Mask undercutting and top of wall punch through. (D) Intact microwells with slight mask undercutting.

The major source of these defects and inconsistencies was likely mounting individual samples onto a carrier wafer rather than having the samples in direct contact the with cryogenic cooling stage. Stable temperature control is critical for cryogenic DRIE of silicon and any deviation from the optimal temperature for a given etching geometry can introduce undercutting and other defects [8]. The Oxford P100 is designed for 4” wafers, and individual samples were mounted to a carrier wafer with vacuum oil which formed an imperfect seal between the samples and carrier wafer. It was noticed that vacuum oil was consumed by the etching plasma which could have

changed the thermal cooling performance throughout longer etching times. Additionally the carrier wafer itself would begin to etch and introduce variation into the process.

The Bosch process can be carried out at room temperature and therefore can avoid thermal management issues of small samples on carrier wafers while etching deep, straight openings in silicon [9]. Several test patterns of microwells were fabricated in plain silicon samples, including 20x20um square microwells of 100um depth separated by 10um sidewalls. A 60x60um square microwell separated by 20um sidewalls was chosen to test on the silicon/pyrex bonded substrates for a direct comparison to samples etched with the cryogenic process. All Bosch process samples exhibited nearly straight sidewalls for the entire depth of the microwells with no undercutting. Samples on the silicon/pyrex substrate stopped etching when the pyrex layer was reached, producing optically transparent microwell arrays (**Figure 4.3**).

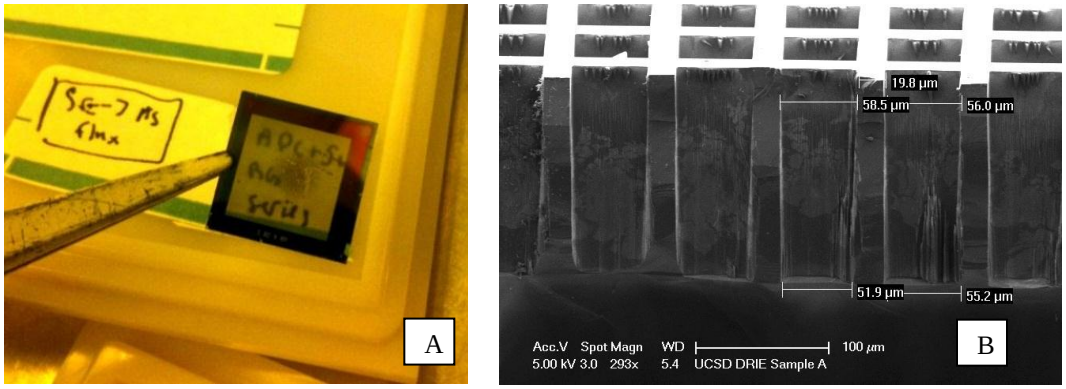

Figure 4.3: (A) Optical transparency of microwell array after etching through to pyrex substrate. (B) Electron microscopy cross section of cleaved sample.

A representative measurement of the dimensions of a microwell was taken near the center of the array; a 58.5 um opening at the top tapered down to 51.9 um at the bottom of the microwell. This 1.89° angle of the sidewall can likely be reduced further with process optimizations. The etching rate was not entirely uniform across the sample surface, leaving approximately 20% of microwells near the center of the chip with a small silicon ring at their bottoms. Slightly extending the etching process time should fully etch the remaining amount of silicon in microwells at the substrate center without affecting the dimensions of microwells around the periphery. The success of fabricating 60x60um square opening microwells of 200um depth on silicon/pyrex substrates along with the previous success of fabricating 20x20um square microwells on plain silicon substrates indicates that 20x20um square microwells of 200um depth should be readily achievable and others have found great success in tuning the Bosch process to wide variety of etching geometries [10]. This would produce microwell arrays of a sufficient depth to opening ratio to limit secretant diffusion on transparent substrates for bottom-up fluorescent imaging.

4.4.2 Live Cell Experiments

To verify that surface markers of cells could be easily stained on-chip without any washing steps which would remove secretants, $5x10^4$ THP-1 cells were plated onto a microarray and allowed to settle for 10 minutes. The cells were incubated with an Alexa488 conjugated MHC-class I antibody for 30 minutes as a positive staining control or with a non-specific Ig antibody as a negative control on separate microwell arrays. The positively stained cells were readily visible without any interfering

background signal. Negative cells were optically transparent and could only be seen on the top walls of microwells were light was reflected (**Figure 4.4a, 4.4b**). To verify that cells could be kept alive over several days to perform time course measurements, cells in culture media were plated onto a microarray and incubated for 5 days at 37°C inside a CO_2 incubator. PI was then introduced to test the viability of cells held in the same culture media for several days. No nonviable cells were found, and the viability test was repeated with the addition of dead cells at the end of 5 days to verify proper PI staining. Both nonviable cells and viable cells are clearly visible (**Figure 4.4c, 4.4d**).

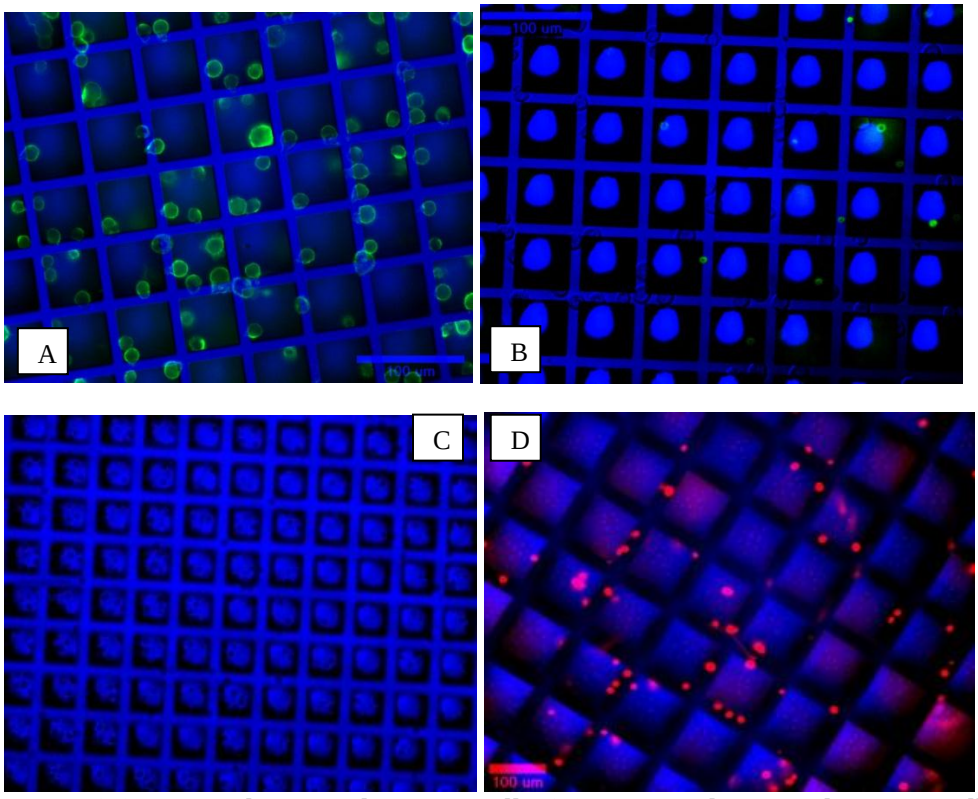

Figure 4.4: (A) Positively stained THP-1 cells (B) Negatively stained THP-1 cells are transparent. (C) Cells incubated for 5 days in media and then incubated with PI. No positively stained cells indicate viability. (D) Cells incubated for 5 days in media, introduced with dead cells, and again stained with PI. Both viable (transparent) and non-viable cells (red) are detected.

4.5 CONCLUSIONS

Bosch process DRIE is a preferable method for deep silicon etching over cryogenic etching when working with small substrates. Silicon microwell fabrication on a transparent substrate shows promise for performing novel live cell experiments by isolating individual cells within their own microenvironment and isolating secretants for automated quantification.

4.6 ACKNOWLEDGEMENTS

Chapter 4, in full, is a reprint of the material as it appears in Material Research Society Symposium Proceedings, vol. 1346, 2011, Martin, David T.; Sandoval, Sergio; Carter, Andy; Rodwell, Mark; Smith, Stefan G. Llewellyn; Kummel, Andrew C.; Messmer, Davorka. The dissertation author was the primary investigator and author of this material.

4.7 REFERENCES

1. C. Czerkinsky, G. Andersson, H.P. Ekre, L.A. Nilsson, L. Klareskog, O. Ouchterlony, "Reverse ELISPOT assay for clonal analysis of cytokine production I. Enumeration of gamma-interferon-secreting cells", *J. of Immunological Methods* 110, 1 (1988).

2. T. Jung, U. Schauer, C. Heusser, C. Neumann, C. Rieger, "Detection of intracellular cytokines by flow cytometry", *J. of Immunological Methods* 159, 1-2 (1993).

3. R. Manz, M. Assenmacher, E. Pfluger, S. Miltenyi, A. Radbruch, "Analysis and sorting of live cells according to secreted molecules, relocated to a cell-surface affinity matrix" *Proc Natl Acad Sci* 92,6 (1995).

4. C. Czerkinsky, Z. Moldoveanu, J. Mestecky, L. A. Nilsson, O. Ouchterlony, "A novel two colour ELISPOT assay. I. Simultaneous detection of distinct types of antibody-secreting cells", *J. Immunol. Methods* 115,1 (1988).

5. A. Rodriguez-Caballero, A. C. Garcia-Montero, C. Bueno, J. Almeida, R. Varro, R. Chen, A. Pandiella, A. Orfao, "A new simple whole blood flow cytometry-based method for simultaneous identification of activated cells and quantitative evaluation of cytokines released during activation", *Lab Invest* 84, 10 (2004).

6. H. Jansen, M. de Boer, H. Wensink, B. Kloeck, M. Elwenspoek, "The black silicon method. VIII. A study of the performance of etching silicon using SF6/O2-based chemistry with cryogenical wafer cooling and a high density ICP source", *Microelectronics Journal* 32, 9 (2001).

7. White, J.G., W.B. Amos, and M. Fordham, "An evaluation of confocal versus conventional imaging of biological structures by fluorescence light microscopy." *The Journal of Cell Biology* 105,1 (1987).

8. M.J. de Boer, J. G. E. Gardeniers, H. V. Jansen, E. Smulders, M.-J. Glide, G. Roelofs, J. N. Sasserath, M. Elwenspoek, "Guidelines for etching silicon MEMS structures using fluorine high-density plasmas at cryogenic temperatures" *Journal of Microelectromechanical Systems* 11, 4 (2002).

9. F. Laerme,., et al. in *Bosch deep silicon etching: improving uniformity and etch rate for advanced MEMS applications*, (Twelfth IEEE International Conference on MEMS '99, Orlando, Florida, 1999).

10. M. J. Walker, "Comparison of Bosch and cryogenic processes for patterning high aspectratio features in silicon", Proc. SPIE 4407 (2001).